Ground State Properties of Neutron-rich Ca Isotopes Measured with Bunched-beam Collinear Laser Spectroscopy

Laurens Bollen

Promotor: Prof. Dr. G. Neyens
Begeleider: J. Papuga

Proefschrift ingediend tot het behalen van de graad van Master of Science in de Fysica

Academiejaar 2012-2013

Dankwoord

Omdat het schrijven van een thesis nooit gelukt zou zijn zonder de hulp en de goede raad van vele anderen, is het niet meer dan logisch om hun te vermelden en hun bijdrage aan dit werk in de verf te zetten.

Allereerst wil ik mijn promotor, prof. dr. Gerda Neyens bedanken. Het spreekt voor zich dat ik u wil bedanken voor het aangename en bijzonder leerrijke jaar waarin ik kon werken aan een boeiend onderwerp. Dat u steeds klaar stond om mijn vragen te beantwoorden en bij te sturen waar nodig heeft daar zeker toe bijgedragen. Bovendien ben ik nog niet vergeten dat u mij enkele jaren geleden definitief heeft overtuigd om mij te verdiepen in kernfysica. Ook daar ben ik u (nog steeds) erg dankbaar voor.

I would also like to thank the other people in the nuclear moments group, for helping me out with problems I encountered on a daily basis. Special thanks go out to Jasna and Ronald.
Jasna, although you were working on different matters, it was clear to me from the start that you wanted to help me out wherever you could. Thanks for giving ideas, answering all my questions and for creating a nice atmosphere.
Ronald, since you were working with the same data, it was of great importance to me that I could also ask you opinion once in a while. That most of our communication was done by e-mail proves how busy you were, but nevertheless I never had to wait long for an answer. Thanks!

Uiteraard wil ik ook de mensen bedanken die er voor mij waren en voor de nodige ontspanning zorgden na een vermoeiende thesisdag of week. Mama en papa, hoewel jullie er nog steeds niet in slagen om de titel van dit werk zonder fout op te zeggen, wil ik jullie bedanken voor de steun die ik steeds ervaarde. Ook wil ik mijn vrienden, die met te veel zijn om op te noemen, bedanken om te zorgen voor wat afleiding en plezier. En Charlotte, bedankt om er altijd voor me te zijn en ook op mindere dagen een glimlach op mijn gezicht te toveren.

Abstract

One of the most important interests in nuclear physics is the establishment of a nuclear structure model that can explain and predict properties of various elements all over the chart of nuclides. These models are based mostly on stable isotopes, as they are prominent and easily produced. Apparently new phenomena appear when nuclei with a deviating neutron-to-proton ratio are taken into account. These exotic nuclei are often radioactive and short-lived, and therefore more difficult to produce and to measure. Nevertheless they are important in astrophysical processes and enable us to gain a better understanding of our universe. Consequently the investigation of properties of exotic nuclei is hot topic in nuclear research.

In this master thesis, neutron-rich calcium ($Z = 20$) nuclei are investigated using collinear laser spectroscopy. This high resolution technique uses laser induced transitions to expose the hyperfine structure of an atom. By optical detection, a spectrum is gathered from which the ground state spin, magnetic and quadrupole moment and differences in mean square charge radii can be obtained. Due to bunching of the ion beam and inserting correlated gates on the photomultiplier tubes, the background is reduced and a high sensitivity is realized. In April 2012, the ground state properties of $^{40,43-52}$Ca were measured at the COLLAPS beam line in ISOLDE, CERN. This work contains the data analysis of this experiment.

As calcium contains 20 protons, which is a magic number, properties of Ca isotopes are mostly determined by the valence neutrons. The most abundant stable Ca isotope also contains 20 neutrons, which makes ^{40}Ca doubly magic. By adding more neutrons, the $1f_{7/2}$ and $2p_{3/2}$ orbitals are filled and expected shell gaps can be investigated. These are manifested by discontinuities in nuclear observables like the nuclear moments or the charge radii. In this experiment, isotope shifts of ^{49,51,52}Ca relative to ^{40}Ca were acquired for the first time. From this, differences in mean square charge radii could be calculated both with an electronic factor

and specific mass shift constant from literature as with our own deduced values. A clear flattening in slope of charge radii was observed before the $N = 28$ shell closure. The potential $N = 32$ shell gap displayed no such effect.

For the first time magnetic moments of ^{49,51}Ca and the quadrupole moment of ^{47,49,51}Ca could be determined using the hyperfine parameters that were obtained from the measured spectra. The experimental nuclear moments were compared to theoretically calculated values using the effective interaction TBLC8. These shell model calculations reproduce both magnetic and quadrupole moments relatively well. On top of the determination of the nuclear moments, the ground state spin of ^{51}Ca was verified to be 3/2, as predicted by theory.

To improve our knowledge on the $N = 32$ shell gap and investigate a possible shell gap at $N = 34$, measurements on ^{53}Ca and ^{54}Ca are in preparation. For this, the experimental beamline needs to be adjusted, because β-detection rather than optical detection should be used to obtain an even higher sensitivity. The possibilities of such an adaptation will be investigated in the following years.

Samenvatting

Eén van de boeiendste thema's in de kernfysica is de zoektocht naar een kernmodel dat in staat is om eigenschappen van alle atoomkernen op de kernkaart te voorspellen en te verklaren. Deze modellen zijn voornamelijk gebaseerd op stabiele isotopen, aangezien zij prominent aanwezig zijn in onze omgeving of makkelijk produceerbaar zijn. Wanneer kernen met een afwijkende neutron-tot-proton verhouding betrokken worden, blijken er echter nieuwe fenomenen te ontstaan. Deze exotische kernen zijn vaak radioactief en hebben een korte vervaltijd, wat het moeilijk maakt om ze te produceren en te bestuderen. Toch zijn ze belangrijk in astrofysische processen en stellen ze ons in staat om ons universum beter te leren begrijpen. Bijgevolg is het onderzoek naar eigenschappen van exotische kernen een actueel onderwerp in kernfysische experimentele activiteiten.

In deze masterproef worden neutronrijke calciumkernen ($Z = 20$) onder de loep genomen met behulp van collineaire laserspectroscopie. Deze hoge resolutie techniek maakt gebruik van laser geïnduceerde transities om de hyperfijne structuur van een atoom te onthullen. Door middel van optische detectie kan een spectrum vergaard worden waarmee de spin, magnetische en quadrupool momenten en verschillen in gemiddelde kwadratische ladingsstraal van de grondtoestand bepaald kunnen worden. Door tijdens het experiment de ionenstraal te bundelen en gecorreleerde tijdgerelateerde poorten over de signalen van de fotondetecotren te zetten, wordt achtergrondruis gereduceerd en kan een hoge gevoeligheid bereikt worden. De meting van eigenschappen van de grondtoestanden van $^{40,43-52}$Ca werd uitgevoerd in ISOLDE te CERN in april 2012. Dit werk bevat de data analyse van dat experiment.

Aangezien calcium 20 protonen bevat, wat een magisch aantal is, zullen eigenschappen van Ca isotopen voornamelijk bepaald worden door het valentie neutron. Het meest voorkomende Ca isotoop heeft eveneens 20 neutronen, wat ^{40}Ca dubbel

magisch maakt. Door steeds meer neutronen bij te voegen zullen de $1f_{7/2}$ en $2p_{3/2}$ orbitalen gevuld worden, en kunnen verwachte schillensluitingen onderzocht worden. Deze openbaren zich door discontinuïteiten in de kernfysische observabelen zoals nucleaire momenten of ladingsstralen. In dit experiment worden de isotoopverschuivingen van ^{49,51,52}Ca in verhouding tot ^{40}Ca voor het eerst verworven. Met deze informatie is het mogelijk om verschillen in gemiddelde kwadratische ladingsstralen te bepalen, gebruik makende van een elektronische factor en specifieke massaverschuivingsconstante. Deze waarden kunnen in de literatuur gevonden worden, of uit ons eigen experiment afgeleid worden. Voor de $N = 28$ schillensluiting kan een duidelijke stagnatie in de trend van ladingsstralen waargenomen worden. Voor de mogelijke schillensluiting op $N = 32$ kunnen we dergelijk effect niet bemerken.

Voor het eerst werden de magnetische momenten van ^{49,51}Ca en de quadrupool momenten van ^{47,49,51}Ca bepaald uit de hyperfijne parameters die we uit de gemeten spectra konden afleiden. De experimentele nucleaire momenten werden vergeleken met theoretische waarden die berekend werden met de TBLC8 effectieve interactie. Deze berekeningen op basis van het schillenmodel konden zowel de magnetische als quadrupool momenten uit het experiment relatief goed benaderen. Bovendien werd ook de spin van ^{51}Ca bepaald. Zoals verwacht uit de theorie is deze 3/2.

Om onze kennis betreffende de $N = 32$ schillensluiting te verbeteren en een eventuele sluiting op $N = 34$ te onderzoeken, zullen in de toekomst experimenten met ^{53}Ca en ^{54}Ca uitgevoerd worden. Hiervoor zal de experimentele opstelling aangepast moeten worden naar een β-detectie systeem in plaats van het huidige optische systeem. De mogelijkheden van zo een modificatie worden momenteel onderzocht.

Contents

List of Figures

List of Tables

Chapter 1

Introduction

The ancient Greeks were the first to mention that matter all around us consists of atoms. The exact meaning of this statement was unclear until Rutherford performed his famous experiment in 1909. He discovered a relatively small region in the atom that was heavy and positively charged, and was later named the nucleus. This composition of protons and neutrons is the complex playground of the nuclear physicist.

The nuclear many body problem was successfully simplified by Mayer and Jensen in 1955 when they proposed the nucleus could be described by an average potential with a shape something between the square well and the harmonic oscillator with a spin orbit term. These assumptions lead to the nuclear shell model, which describes the nucleus as a system of protons and neutrons that are arranged in quantum orbitals. In most cases, such a system is described as a core nucleus with one or more valence nucleons around it. Note that this is analogous to the more convenient picture in atomic physics, where electrons move in orbitals induced by the Coulomb field of the nucleus. In both shell models, the properties of the system are mostly determined by the valence particle(s). One of the early huge successes of this model is the explanation of so-called magic numbers. When there is a quantity of protons or neutrons consistent with a magic number (2, 8, 20, 28, 50, 82 or 126), the nucleus tends to be very stable and large energy gaps can be observed between the subsequent quantum orbits. More than ten years after the discovery of magic numbers [1], the nuclear shell model was the first theoretical basis to give a decent explanation to this phenomenon.

As for today, it is still impossible to solve the nuclear many body problem exactly. Therefore, models containing two body interactions between nucleons on top of the central potential are a huge topic of interest for theoreticians. To review and extend their models, they are in need of experimentalists that provide them with information to test the predictions made by nuclear structure calculations. These experimental observables contain mass, nuclear moments, spin, excitation energies, charge radii and so on. The interaction between theory and experiment enables us to approach a complete picture of nuclear systems more closely.

During this process of constant refinement of nuclear models, a number of intriguing new properties in various regions of the nuclear chart have been discovered. A certain source of interest are the so called exotic nuclei, which are isotopes with a large neutron excess or deficiency. These nuclei are in most cases less stable and therefore have a shorter lifetime. Observed phenomena such as the appearance of new magic numbers rises questions about the exact composition of the wavefunctions of exotic nuclei. To gain insight into this matter, a reliable experimental technique has to supply the mentioned observables.

In this work, neutron rich calcium isotopes ($Z = 20$) are studied using a collinear laser spectroscopy technique. This high resolution technique enables us to survey the ground state properties of Ca isotopes up to $A = 52$. A beam of ions is excited by a laser tuned at the transition frequency between two atomic levels. Photons are emitted when the ions deexcite and are collected in photomultiplier tubes. Due to hyperfine interactions the atomic levels are split into hyperfine levels. By scanning the frequency of the laser light over a small region, the hyperfine parameters and transition frequency can be obtained from the photon spectra. Using a bunching technique, the signal-to-noise ratio is improved by 4 orders of magnitude and a very high sensitivity is obtained. The result of the experiment is described in this thesis.

The next chapter contains a brief motivation of the research in this work. It is both an answer to the question "Why investigate exotic Ca nuclei?", as an introduction to the data analysis and the expected results. In Chapter 3, the main physical concepts and notions are dealt with. This includes isotope shifts, mean square charge radii, nuclear moments and hyperfine interactions. Chapter 4 handles the experimental technique, collinear laser spectroscopy, both in a theoretical and an applicable way. Next, the summary of the data and analysis procedure are described in Chapter 5. In Chapter 6 the final results are reported and discussed. As a conclusion the most important realizations are summarized, and some future outlooks are given.

Chapter 2

Motivation

In this chapter the importance of studying neutron rich calcium nuclei will be highlighted, and the physics case will be outlined. Therefore it is important to understand why calcium isotopes are interesting and what one can deduce from their properties.

Calcium has 20 protons, which is a magic number. As the stable ^{40}Ca isotope also has 20 neutrons, it is called doubly magic. By adding neutrons other calcium isotopes are formed. In this experiment isotopes ranging from $A = 43$ to $A = 52$ are considered. The schematic structure of these isotopes according to the shell model can be seen in Figure 2.1. Note that ^{48}Ca is also a doubly magic nucleus.

As Ca isotopes with an even number of neutrons are even-even nuclei, they will have a nuclear spin zero in the ground state. The spin and parity of odd-A Ca isotopes will be determined by the valence neutron(s). This means the spin/parity of isotopes 43, 45 and 47 is expected to be $7/2^-$ due to the single unpaired neutron in the $f_{7/2}$ shell. This has been confirmed by experiments [2]. Thereafter the $p_{3/2}$ shell is filled, and consequently the spin/parity for ^{49}Ca and ^{51}Ca is expected to be $3/2^-$. This is experimentally confirmed for ^{49}Ca [2] and theoretically predicted for ^{51}Ca [3]. As collinear laser spectroscopy is a technique suitable to deduce the spin, both directly and by comparing trends of nuclear moments, confirming the spin of ^{51}Ca is one of the goals of this experiment.

Another part of interest is the shell structure beyond $N = 28$ [4]. There is experimental evidence for a sub-shell closure at $N = 32$ [5, 6, 7, 8, 9], and theoretical predictions based on shell-model calculations (the GXPF1A interaction) for the
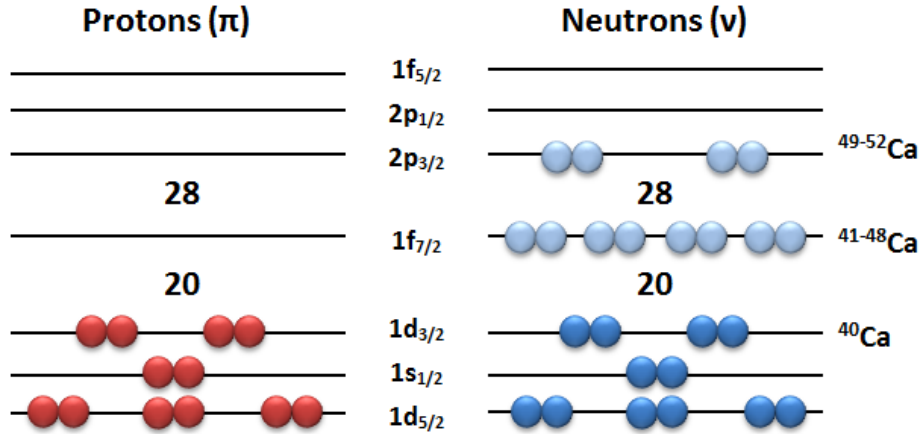
Figure 2.1: The configuration of the proton and neutron shells for the Ca isotopes. With increasing neutron number the $1f_{7/2}$ and $2p_{3/2}$ neutron levels are subsequently filled.

fp-shell also predict such a closure at $N = 34$ [10]. At the same time, shell model calculations using the KB3G interaction [11] only support a $N = 32$ shell closure, and no closure at $N = 34$. Although indirect experimental evidence has recently been reported by Maierbeck *et al.* [12], there is no direct experimental evidence yet. On the other hand, Beiner *et al.* already predicted this closure over 30 years ago [13]. This discussion concerning the shell evolution, that is the change of the shell structure due to the occupation of single-particle orbits, can be presented by plotting the 2^+ excitation energies for every even-even Ca isotope, as in Figure 2.2. There is a remarkable rise in excitation energy from $N = 30$ to $N = 32$, but predicted behavior at $N = 34$ depends on the effective interaction that is used. The lack of experimental data limits a full understanding of this matter.

The magicity of proton and neutron numbers is manifested by discontinuities in nuclear observables. This can be a sudden increase in energy of the first excited 2^+ state, but also a raised neutron separation energy, a characteristic change of slope in mean square charge radii, an increase of the magnetic moment towards the Schmidt value, a decrease in absolute value of the quadrupole moment and so on. This sensitivity can be used to examine the strength of the $N = 32$ sub-shell closure. In Figure 2.3 this is illustrated by the root mean square charge radii of isotopes in the vicinity of the $N = 28$ closure.

Laser spectroscopy is a proper technique to get information on nuclear spin, moments and charge radii, because it is a high resolution technique which can provide
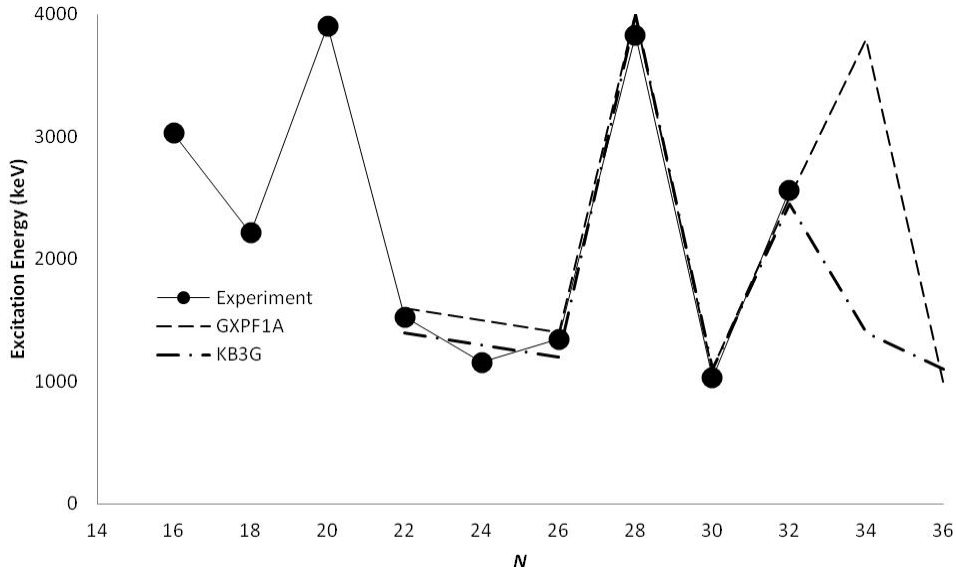
Figure 2.2: 2^+ excitation energies of Calcium isotopes compared with 2 theoretical predictions generated with the shell model interactions GXPF1A and KB3G. GXPF1A predicts an increase in the gap with neutron number up to $N = 34$ in Ca, KB3G demonstrates no such effect. [14, 15]

model independent information. In this experiment only the calcium isotopes up to $N = 32$ will be investigated, but at a later point the goal should be to measure the properties up to $N = 34$. By measuring the magnetic moment and comparing it to calculated single particle moments, information on the composition of the wave function of the nucleus can be extracted. From comparison of experimental moments and calculated moments using an effective interaction, shortcomings of the nuclear models in the calcium region can be discovered and improved.

To conclude this chapter, the goals of this experiment are summarized:

- Measure the differences in mean square charge radii between ^{40}Ca and $^{43-52}$Ca. The differences in mean square charge radii of ^{49,51,52}Ca will be measured for the first time.

- Measure the nuclear magnetic moment of ^{43,45,47,49,51}Ca. The magnetic moments of ^{49}Ca and ^{51}Ca have never been observed before.

- Measure the nuclear quadrupole moment of ^{43,45,47,49,51}Ca. For the first time, the quadrupole moment of ^{47,49,51}Ca will be determined.

- Confirm the spin of ^{51}Ca experimentally.
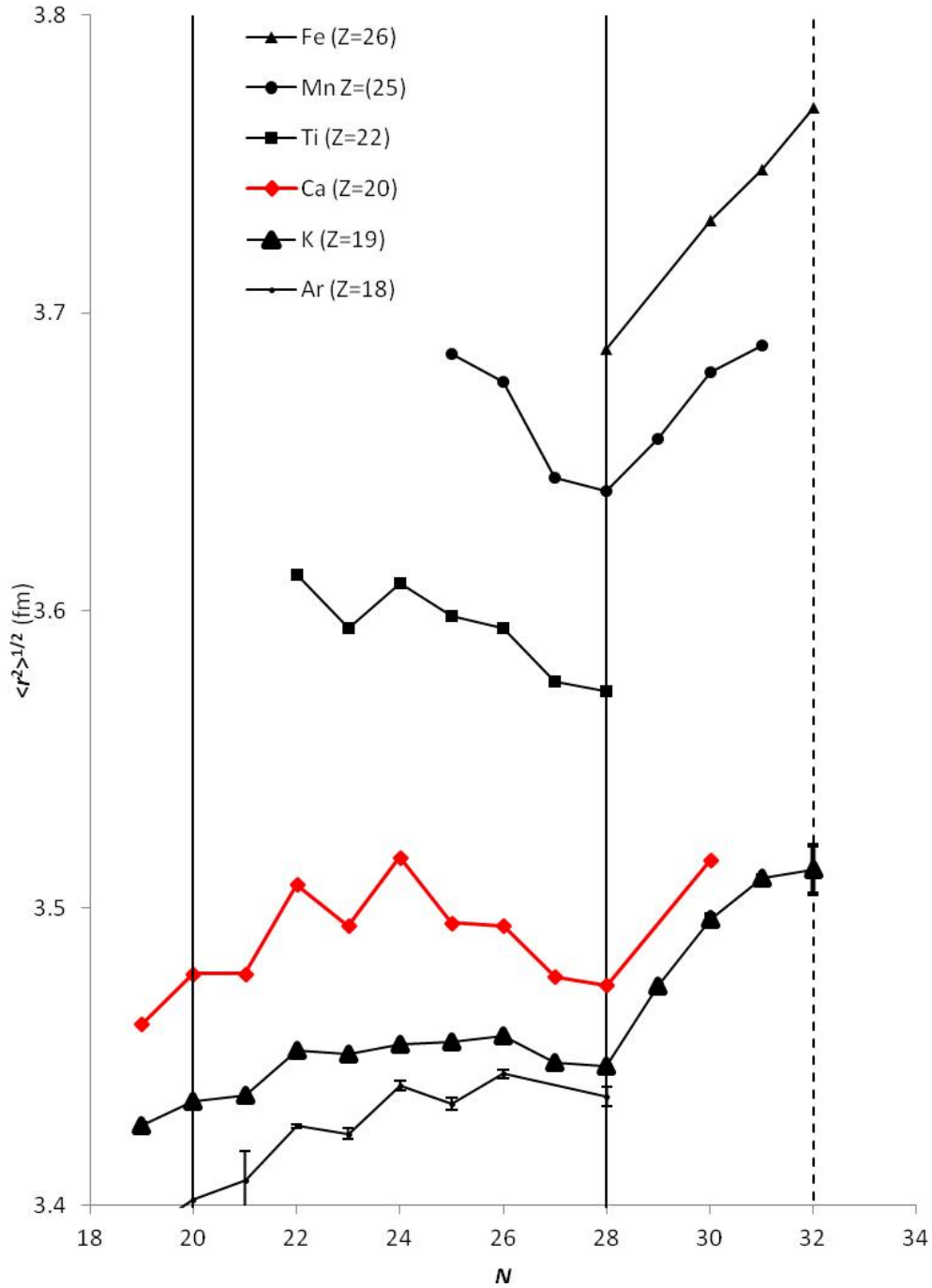
Figure 2.3: Root mean square charge radii in the calcium region [14, 16, 17]. There is a larger odd-even staggering effect in the isotopic chain of Ca than in that of K ($Z = 19$). This can be understood in terms on the blocking effect of the single unpaired proton in K. Therefore, the sensitivity to a shell effect at $N = 32$ would be increased in Ca. When combining the Ca results with the full K and Mn ($Z = 25$) measurements, the variation of the influence of $N = 32$ can be fully explored.

Chapter 3

Theoretical and Experimental Observables

The goal of this kind of research is to learn more about the configuration of the wave function of the ground state of the nucleus, the deformation of the nuclei, the interactions between the nucleons and so on. Unfortunately, one cannot measure these properties in a straightforward way. Using collinear laser spectroscopy observables concerning the nuclear moments and interactions with the electron cloud are used to extract information about the above mentioned characteristics of the nuclei. This chapter is a theoretical guideline to these nuclear observables.

3.1 The nuclear multipole moments

Electromagnetic moments are very important in nuclear physics due to their sensitivity to nuclear structure. By measuring them it is possible to gain insight in the way nucleons interact in many-particle systems. The nuclear charge radius, magnetic moment and quadrupole moment are therefore crucial to understand the nature of nuclear states.

3.1.1 The nuclear mean square charge radius

When discussing the nuclear radius it is important to mention the well known 'liquid drop model' equation [18]

$$r = R_0 A^{1/3}, \tag{3.1}$$

with $R_0 \sim 1.2$ fm a proportionality constant and A the mass number of the atom. However, the nuclear radius is not such a well-defined quantity, as there can be many involving interactions. This is why the nuclear mean square charge radius is preferable. It is defined as [19]

$$\langle r^2 \rangle = \frac{\int \rho(\mathbf{r}) r^2 d^3 r}{\int \rho(\mathbf{r}) d^3 r}$$

where $\rho(\mathbf{r})$ is the charge distribution. The denominator is then just a normalization factor given by the nuclear charge, Ze. This quantity can in fact be considered as a monopole moment of the nucleus. Returning to the liquid drop model, the nuclear mean square charge radius can also be written as [20]

$$\langle r^2 \rangle = \frac{3}{5} r^2 = \frac{3}{5} R_0^2 A^{2/3}$$

In the region between two closed nucleon shells, deformed, non-spherical nuclei exist. These deformations give rise to an extra deformation parameter β, which is defined by the angular dependence of the length of the radius vector to the nuclear surface expressed in spherical harmonics. It is connected to the mean square charge radius as follows [19]:

$$\langle r^2 \rangle = \frac{3}{5} R^2 + \frac{3}{4\pi} R^2 \beta^2 \tag{3.2}$$

This can be rewritten, assuming that $\langle r^2 \rangle_{\text{sph}}$ is the mean square charge radius of a spherical nucleus with the same volume:

$$\langle r^2 \rangle = \langle r^2 \rangle_{\text{sph}} (1 + \frac{5}{4\pi} \beta^2)$$

The mean square charge radius gives information on the charge distribution and charge deformation. In practice the isotope shift will be measured to get the difference in mean square charge radii between isotopes. This difference can be written as

$$\delta \langle r^2 \rangle^{A,A'} = \langle r^2 \rangle^{A'} - \langle r^2 \rangle^A \tag{3.3}$$

With A and A' the isotopes of interest.

3.1.2   The nuclear magnetic dipole moment

The nuclear magnetic moment is caused by two phenomena. On one hand there is a contribution from the orbiting positively charged protons. This orbiting motion gives rise to an orbital magnetic moment just like in classical mechanics. On the other hand there is also a contribution from the intrinsic spin of all nucleons, the

intrinsic magnetic moment. Together they form the expression for the nuclear magnetic dipole operator [21]:

$$\boldsymbol{\mu} = \sum_{i=1}^{A} g_l^i \mathbf{l}^i + \sum_{i=1}^{A} g_s^i \mathbf{s}^i$$

where $\mathbf{l}^i$ and $\mathbf{s}^i$ are the orbital and spin angular momentum gyromagnetic factors of the ith nucleon respectively, while the sum ranges over all nucleons. The g-factors for the nucleons are [21]

$$\text{For protons: } g_l = 1 \text{ and } g_s = +5.586$$
$$\text{For neutrons: } g_l = 0 \text{ and } g_s = -3.826$$

This means that the neutron has a nonzero magnetic moment, and because it is uncharged, this indicates that it must have some internal structure.

The magnetic dipole moment $\mu(I)$ is the expectation value of the z-component of the dipole operator $\boldsymbol{\mu}$:

$$\mu(I) = \langle I, m = I | \boldsymbol{\mu}_z | I, m = I \rangle$$

This is connected with the nuclear spin via the gyromagnetic ratio:

$$\mu = g_I I \mu_N$$

Where μ_N is the nuclear magneton and g_I the g-factor of a nucleus with nuclear spin I,

$$\mu_N = \frac{e\hbar}{2m_p} \approx 0.105155e \text{ fm}$$

The properties of odd-even nuclei near closed shells are described by the characteristics of the unpaired valence nucleon. This means the magnetic moment of such a state can be calculated. If the valence nucleon is in an orbit with total angular momentum j and orbital momentum l, the magnetic moment of the free nucleon can be calculated using the formula for the Schmidt moments [22]:

$$\mu(l + \frac{1}{2}) = \left[(j - \frac{1}{2})g_l + \frac{1}{2}g_s \right]$$
$$\mu(l - \frac{1}{2}) = \frac{j}{j+1} \left[(j + \frac{3}{2})g_l - \frac{1}{2}g_s \right] \tag{3.4}$$

The measured magnetic moments of valence nucleons differ from the calculated values because of the interaction with other nucleons in the nucleus. This can be accounted for by introducing an effective g-factor. Therefore g_s is reduced to typically 70 to 90% of its free value.

3.1.3 The nuclear electric quadrupole moment

The deviation of the nuclear charge distribution from a spherical form gives rise to a nuclear electric quadrupole moment. The quadrupole operator in the Cartesian system is [20]

$$\mathbf{Q_z} = \sum_{i=1}^{A} e_i(3z_i^2 - r_i^2)$$

where e_i is the nucleon charge: zero for neutrons, $+e$ for protons. This means the quadrupole moment is completely determined by the motion of the protons in the nucleus. However, due to the strong interaction between all nucleons, neutrons will also indirectly contribute to the quadrupole moment. In a spherical bases one can express $\mathbf{Q_z}$ as a zero-order component of a rank 2 tensor:

$$\mathbf{Q_z} = \sqrt{\frac{16\pi}{5}} \sum_{i=1}^{A} e_i r_i^2 Y_2^0(\theta_i, \phi_i)$$

In experiments, the spectroscopic quadrupole moment is observed, which is the expectation value of the quadrupole operator.

$$Q_s(I) = \langle I, m = I | \mathbf{Q_z} | I, m = I \rangle = \sqrt{\frac{I(2I-1)}{(2I+1)(2I+3)(I+1)}} \langle I \| \mathbf{Q_z} \| I \rangle$$

One should note that for $I < 1$ this expression, and thus the quadrupole moment, is equal to zero. The conclusion here is that although a nucleus with spin $I = 0$ or $I = 1/2$ can have an intrinsic deformation, it is not possible to measure the quadrupole moment.

The spectroscopic quadrupole moment Q_s can be related to the intrinsic quadrupole moment Q_0. Assuming the nuclear deformation to be axially symmetric and the nuclear spin to have a well-defined direction with respect to the symmetry axis, it is possible to calculate the relation between the spectroscopic an the intrinsic quadrupole moment. Although these assumptions are not always valid, they are often made in the strong coupling case [20]. The relation turns out to be:

$$Q_s = \frac{3K^2 - I(I+1)}{(I+1)(2I+3)} Q_0$$

where K is the projection of the nuclear spin on the deformation axis. The intrinsic quadrupole moment Q_0 can also be related to the nuclear charge deformation β [20]:

$$Q_0 = \frac{3}{\sqrt{5\pi}} Z r^2 \beta (1 + 0.36\beta)$$

With r defined as in (3.1) and β related to the mean square charge radius as in (3.2).

Similarly as with the nuclear dipole moment, it is possible to find an equation for the spectroscopic quadrupole moment for a system consisting of a single valence proton outside a closed shell ($Q_{s.p.}$). Therefore one has to make a decomposition of the single particle wave function into spin, radial and orbital parts. The effective single particle quadrupole moment for a proton in an orbital with total angular momentum j turns out to be

$$Q_{s.p.}^{\text{eff}} = -e_j \frac{2j-1}{2j+2} \langle r_j^2 \rangle \tag{3.5}$$

With e_j the effective charge of the nucleon in orbital j, and $\langle r_j^2 \rangle$ the mean square charge radius in that orbital. Note that neutrons have no charge, and therefore do not induce a single particle quadrupole moment. However, neutrons in a nucleus interact with nucleons in the core. This means that the core can be polarized, what is accounted for in the effective charge of the nucleons. The value of the effective charge depends on the model that is used. In this work the TBLC8 interaction [23] is used ($e_p^{\text{eff}} = 1.5e$ and $e_n^{\text{eff}} = 0.5e$, and $e_p^{\text{eff}} = 1.486e$ and $e_n^{\text{eff}} = 0.84e$). Note also that the minus sign shows that the quadrupole moment is negative for a single particle orbiting a closed shell. The core polarization induced by this particle will lead to an oblate ellipsoid. In the same way a single hole in a closed shell will lead to a positive quadrupole moment, and a prolate charge distribution (Figure 3.1).
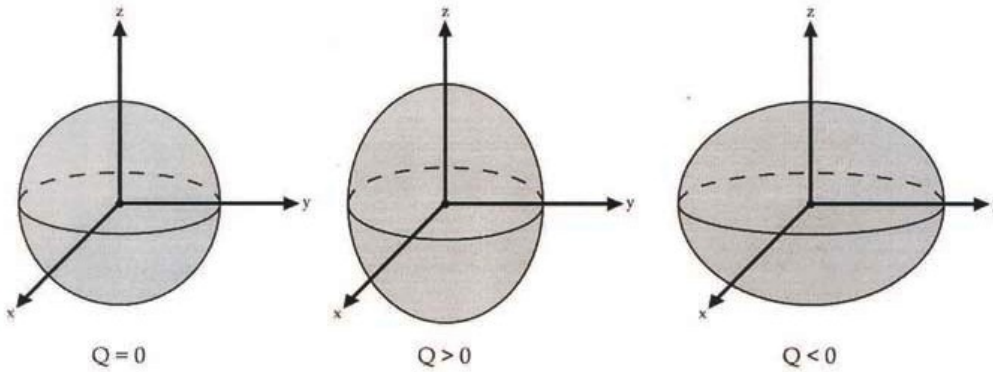
Figure 3.1: A spherical nucleus and a prolate ($Q > 0$) and oblate ($Q < 0$) deformation. [24]

3.2 Interactions of nuclear moments with orbital electrons

When investigating the interactions of the nuclear moments with the electromagnetic fields in the surroundings of the nucleus, one can measure the static moments of nuclei. These electromagnetic fields can be induced by orbital electrons, or by neighboring nuclei and their electrons when the nuclei are implanted in a crystal. It is also possible that there is an external magnetic field present. Different moments interact with different parts of the electromagnetic fields surrounding the nucleus.

3.2.1 The isotope shift

The radial nuclear charge distribution interacts with the orbital electrons, inducing an small ($\sim \mu$eV) shift in the atomic transition frequencies, which will give rise to the monopole term in the interaction Hamiltonian. This energy shift is different for each isotope and is therefore called the isotope shift. There are two contributions to this isotope shift: the mass shift and the field shift. Consequently, the isotope shift can be written as a difference in frequencies, or as a sum of two contributions:

$$\delta\nu^{A,A'} = \nu^{A'} - \nu^{A} \tag{3.6}$$

$$\delta\nu^{A,A'} = \delta\nu^{A,A'}_{\text{mass shift}} + \delta\nu^{A,A'}_{\text{field shift}} \tag{3.7}$$

A and A' are the atomic masses of involved isotopes and ν is the transition frequency between two fine structure levels.

The mass shift

The center of mass in an isotope is determined by the number of nucleons and the number of orbiting electrons. The motion of electrons and the nucleus will thus be different for every isotope. This gives rise to a mass shift. The mass shift can be split further into two contributions: the normal mass shift (NMS) and the specific mass shift (SMS) [25].

$$\delta\nu^{A,A'}_{\text{mass shift}} = \delta\nu^{A,A'}_{\text{NMS}} + \delta\nu^{A,A'}_{\text{SMS}}$$

This can be rewritten as a sum of two coefficients, proportional to the reduced mass:

$$\delta\nu^{A,A'}_{\text{mass shift}} = \frac{m_{A'} - m_A}{m_A(m_{A'} + m_e)}(K_{\text{NMS}} + K_{\text{SMS}}) \tag{3.8}$$

The normal mass shift is related to reduced mass of the nucleus-electron system, and its coefficient (K_{NMS}) can be written as the product of the electron mass and

the transition frequency:

$$K_{\text{NMS}} = m_e \nu_0^A \tag{3.9}$$

The specific mass shift is due to the changes in the interaction between the electrons, its coefficient (K_{SMS}) depends on the electronic structure of the system. Note that the mass shift is inversely proportional to m^2. This means that the contribution of the mass shift reduces fast for heavy nuclei, and thus is most important for light atoms.

The field shift

Changes in the volume and the shape of the nuclear charge distribution will cause a change of the field interactions between electrons and the nucleus. This is due to a probability of overlap between the s and $p_{1/2}$ electron orbitals with the nucleus. The field shift is thus in fact a correction on the monopole energy which does not lift any degeneracies, but only shifts the energy levels. This depends on the amount of penetration and the mean square charge radius of the nucleus. The nuclei of different isotopes have different nuclear radii, and thus will account for different corrections. This can be converted into an equation [26]:

$$\delta\nu^{A,A'}_{\text{field shift}} = F(\delta\langle r^2\rangle^{A,A'} + \frac{C_2}{C_1}\delta\langle r^2\rangle^{A,A'} + ...) \tag{3.10}$$

Here F is an electronic factor which depends on the electronic structure of the atomic levels and $\delta\langle r^2\rangle^{A,A'}$ is the difference of the nuclear mean square charge radius between two isotopes A and A', as it is given in equation (3.3). For light elements equation (3.10) reduces to

$$\delta\nu^{A,A'}_{\text{field shift}} = F\delta\langle r^2\rangle^{A,A'} \tag{3.11}$$

The field shift $\delta\nu^{A,A'}_{\text{field shift}}$ is proportional to the atomic number Z. This means that it will increase for heavier nuclei. As stated before, the mass shift will reduce when looking at heavy elements. In order to get information on the mean squared charge radius it is challenging and necessary to investigate which effects are due to the field shift, and which are due to the mass shift [25].

3.2.2   The hyperfine interactions

An atomic nucleus is not an isolated system, but is surrounded by electrons. The nuclear moments will therefore interact with the fields that are generated by these atomic electrons. There are different contributions of these interactions, which can be separated when making a multipole expansion of the interaction Hamiltonian:

$$H_{\text{interaction}} = H(E0) + H(M1) + H(E2) + ... \tag{3.12}$$

Where $H(E0)$ is the electric monopole, $H(M1)$ the magnetic dipole and $H(E2)$ the electric quadrupole interaction. The monopole interaction is the architect of the atomic energy levels, with a correction for the isotope shift that was discussed before. The higher order contributions are called the hyperfine interactions. It might be helpful to place these interactions in context, when looking at Figures 3.2 and 3.3. The hyperfine interactions only make a small difference in energy ($\sim \mu$eV), although it is a vital contribution. [24]
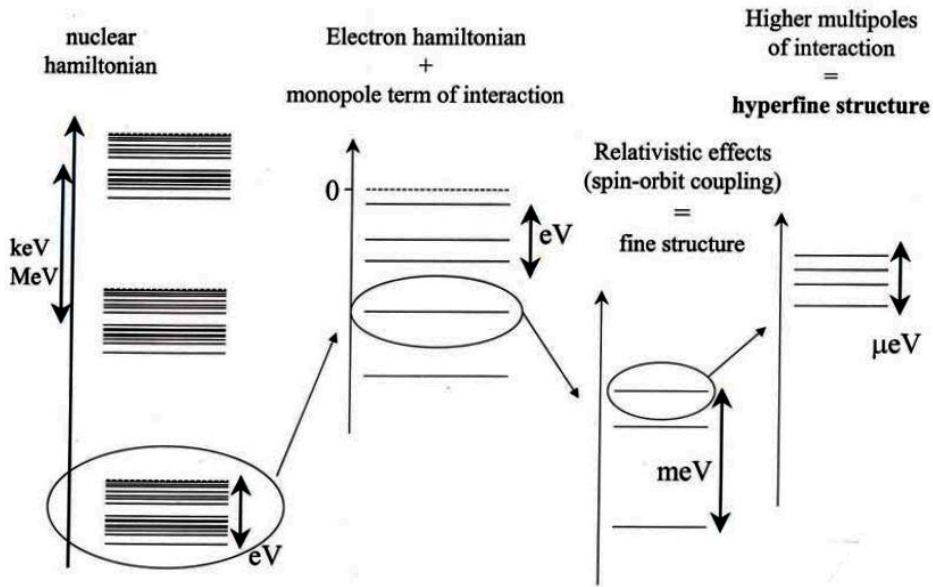
Figure 3.2: Schematic representation of the different energy scales of the nucleus-electrons system interaction. From left to right: different nuclear states yield a separation of keV or MeV. Interactions between the electrons and a nuclear point charge, and between the electrons themselves give corrections of the order of eV (atomic energy levels). When relativistic effects are added, the spin-orbit coupling is responsible for the fine structure ($\sim$meV). If further multipole interactions between nucleus and electrons are added, splittings of the order of $\sim \mu$eV are introduced, and a hyperfine structure is created. This hyperfine structure can vary for different nuclear states, which makes it an small but important contribution in the energy spectra. [24]

In order to better understand and to simplify the mathematical description, there is a general procedure to introduce a new quantum number: the total angular momentum of the nucleus-electron system F. This is the coupling of the electronic

$$
\begin{array}{c|c|c|l}
\hat{T}_n \otimes \mathbb{1} + \hat{U}_{nn} \otimes \mathbb{1} & T_n + U_{nn} & keV - MeV & nuclear\ energy\ levels \\
\mathbb{1} \otimes \hat{T}_e + \mathbb{1} \otimes \hat{U}_{ee} + \hat{Q}^{(0)} \otimes \hat{V}^{(0)} & T_e + U_{ee} + E_{ne}^{(0)} & eV\ (meV) & atomic\ energy\ levels \\
\hat{Q}^{(1)} \otimes \hat{V}^{(1)} + \hat{Q}^{(2)} \otimes \hat{V}^{(2)} & E_{ne}^{(1)} + E_{ne}^{(2)} & \mu eV & hyperfine\ structure
\end{array}
$$

Figure 3.3: Schematic representation of the different terms in the total Hamiltonian of the system nucleus + electrons. The nucleon-nucleon interaction and the kinetic energy of the nucleons are responsible for the keV and MeV energy separations. The kinetic energy of the electrons, electron-electron interaction and monopole term of the electron-nucleus interaction introduce the eV splittings. The fine structure ($\sim$meV) may be present if relativistic effects are taken into account. The higher order multipole terms of the electron-nucleus interactions are responsible for the hyperfine structure, which accounts for energy splittings in the order of μeV. [24]

angular momentum J and the nuclear spin I:

$$
\mathbf{F} = \mathbf{J} + \mathbf{I} \tag{3.13}
$$

where F takes values from $|I - J|$ until $I + J$ with steps of 1. This means that the hyperfine interaction gives rise to a splitting into $2J + 1$ levels for $J < I$ or $2I + 1$ levels for $I < J$. Allowed energy transitions are given by the selection rule:

$$
\Delta F = 0, \pm 1 \tag{3.14}
$$

with an exception of the energy transition between two $F = 0$ states, which is not allowed. It is now possible to split the discussion into two parts: the magnetic and the quadrupole hyperfine interaction, as it was shown in the Hamiltonian in equation (3.12).

The magnetic dipole interaction

The part of the Hamiltonian in (3.12) that accounts for the magnetic dipole interaction can be written as

$$
H(M1) = -\boldsymbol{\mu}\mathbf{B}(\mathbf{0})
$$

with $\boldsymbol{\mu}$ the nuclear magnetic moment operator, and $\mathbf{B}(\mathbf{0})$ the magnetic field operator of the electrons at the position of the nucleus. The energy difference between the fine structure level and the hyperfine state is given by

$$
\Delta E_M = \frac{AC}{2} \tag{3.15}
$$

with A the magnetic dipole hyperfine parameter, given by the formula

$$A = \frac{\mu B}{IJ} \tag{3.16}$$

and C is just introduced to simplify the notation:

$$C = F(F+1) - I(I+1) - J(J+1) \tag{3.17}$$

As can be seen from equation (3.16) the connection between the nuclear dipole moment μ and the hyperfine splitting is proportional to the A-factor. Note that neither $I = 0$ or $J = 0$ is allowed in this description, as a nucleus with spin $I = 0$ does not have a magnetic moment, and $B(0)$ is proportional to J.

The electric quadrupole interaction

The nuclear electric quadrupole moment is due to the non-spherical shape of the nucleus, as stated before. The quadrupole moment will interact with an electric field gradient, generated by the electrons. This gives rise to another splitting in the atomic energy levels, which can only occur for nuclei with $I \geq 1$, because otherwise there is no electric quadrupole moment present. The splitting in the energy levels is proportional to the electric quadrupole hyperfine parameter B (or B-factor):

$$\Delta E_Q = B\frac{\frac{3}{4}C(C+1) - I(I+1)J(J+1)}{2I(2I-1)J(2J-1)} \tag{3.18}$$

With C given by equation (3.17). The B-factor is related to the quadrupole moment as follows:

$$B = eQ_sV_{zz}(0)$$

Where e is the elementary electron charge, Q_s the spectroscopic nuclear quadrupole moment (given in barns or fm^2) and $V_{zz}(0)$ the z-component of the electric field gradient of the orbital electrons at the position of the nucleus. It can be verified that for $I = 0$ and $I = 1/2$ the denominator in equation (3.18) is equal to zero. This is understandable since for $I < 1$, the quadrupole moment is equal to zero. The second condition is that $J \geq 1$, otherwise the B-factor is zero because $V_{zz}(0) = 0$ for $J = 0$.

From equations (3.15) and (3.18) the hyperfine structure energy of a certain level F of a hyperfine structure multiplet can be obtained. It is described in terms of the atomic fine structure level J and the nuclear spin I as follows:

$$E_F = \frac{AC}{2} + B\frac{\frac{3}{4}C(C+1) - 2I(I+1)J(J+1)}{2I(2I-1)J(2J-1)} \tag{3.19}$$

3.3 Determination of nuclear moments

The A- and B-factors are used to obtain values for the nuclear moments. Experimentally, transition frequencies are determined and therefore, the A- and B-factor are measured in frequency units (MHz). Instead of using direct measurements, nuclear moments are calculated on a relative base:

$$\mu = \frac{AI}{A_{\text{ref}}I_{\text{ref}}}\mu_{\text{ref}} \tag{3.20}$$

$$Q = \frac{B}{B_{\text{ref}}}Q_{\text{ref}} \tag{3.21}$$

All quantities with a 'ref' subscript are taken from earlier measurements or calculations that were found in literature. The other quantities are experimentally obtained.

In our analysis, ^{43}Ca is used as a reference isotope because it is the only stable odd isotope, and its nuclear moments and hyperfine parameters were determined with various methods. The reference number for the A-factor was obtained by Arbes *et al.* [27] with high precision using a laser microwave double resonance technique. Its nuclear magnetic moment was determined by Lutz *et al.* [28] using nuclear magnetic resonance. The hyperfine parameter B_{ref} is defined as the weighted mean (equation (5.5)) of our B parameter and the B parameters measured by Nörtershäuser *et al.* [29] and Silverans *et al.* [30], both using collinear laser spectroscopy. The error on this value is the maximum of the statistical and scattering error of these values (formulae (5.6) and (5.7)). The reference value for the quadrupole moment is obtained by a finite element multiconfiguration Hartree-Fock determination by Sundholm and Olson [31]. An overview of these reference values can be found in Table 3.1.

^{43}**Ca**		**ref.**
$\mathbf{A}_{\text{ref}}$	-806.4020716(8) MHz	[27]
$\boldsymbol{\mu}_{\text{ref}}$	-1.317643(7) μ_N	[28]
B_1	-4.8(1.9) MHz	our value
B_2	-6.9(1.7) MHz	[29]
B_3	-6.7(1.4) MHz	[30]
$\mathbf{B}_{\text{ref}}$	-6.28(94) MHz	
$\mathbf{Q}_{\text{ref}}$	-0.0408(8) b	[31],[32]

Table 3.1: The reference values for ^{43}Ca used for the determination of the nuclear moments. For the B parameters, the weighted of three independent measured values was used as the reference value.

Chapter 4

Experimental Setup

In this chapter the experimental techniques and setup will be described. First, basic information of the ISOLDE facility is given. Afterward, the COLLAPS beam line and the principles of the collinear laser spectroscopy technique are discussed in more detail.

4.1 ISOLDE facility at CERN

The experiment was performed at CERN (research lab in Geneva, Switzerland) in the ISOLDE hall (Isotope Separation On-Line DEvice). The on-line isotope mass separator ISOLDE is a facility dedicated to the production of a large variety of radioactive ion beams for many different experiments in the fields of nuclear and atomic physics, solid-state physics, materials science and life sciences. A beam of radioactive isotopes is produced by impinging $1.0 - 1.4$ GeV protons with an intensity up to 2 μA from the Proton Synchrotron Booster on a certain target, for example uranium carbide UC_2. The protons impinging the target induce spalation, fission and fragmentation reactions. More than 600 isotopes with half-lives down to milliseconds of almost 70 elements ($Z = 2$ up to 88) have been produced at intensities up to 10^{11} atoms per μA proton beam. [33]

After diffusion out of the target, an ion source is used to ionize the element of interest. There are three possible ion sources: the Resonance Ionization Laser Ion Source (RILIS), surface ionization source and plasma ionization source. In this experiment, RILIS was used to ionize the calcium atoms. Afterward, the ions are accelerated and mass separated. ISOLDE uses two different separators: the

General Purpose Separator (GPS), designed to allow three different beams within a certain mass range to be selected and delivered simultaneously into the experimental hall via three different beam lines, and a High Resolution Separator (HRS) which can only deliver one mass at a time to the experimental hall.

In Figure 4.1 the process of the radioactive ion beam production is summarized into four stages. Most of the experiments study the structure of the nucleus in different ways, but there are also experiments relevant to atomic physics, nuclear astrophysics, fundamental physics, solid-state physics and life sciences. In the experiment that is relevant for this thesis, the beam will be delivered to the COL-LAPS beam line. [34]
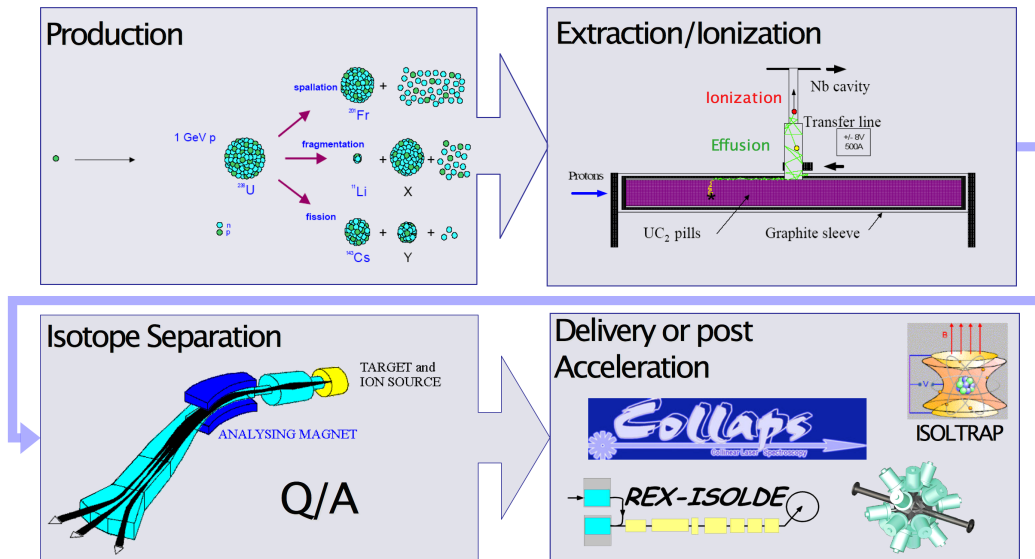
Figure 4.1: The main stages of radioactive ion beam production at ISOLDE. [33]

4.2   Collinear laser spectroscopy at ISOLDE

In this section the experimental assembly used to investigate the spins, moments and charge radii of exotic nuclei will be discussed. First, a theoretical approach will clarify the goal and the strength of the collinear laser spectroscopy technique. Afterward, a description of the implementation at CERN is given.

4.2.1 Theoretical aspects of the technique

Collinear laser spectroscopy is a very powerful high-resolution technique to measure nuclear multipole moments and differences in mean square charge radii. First the ion beam from ISOLDE is superimposed on a narrow-band laser beam by an electric deflector. The laser frequency can be swept over multiple values. When this frequency is in resonance with an ionic (or sometimes atomic) transition from the ground state, an excitation takes place. All this can be detected by observing the fluorescence light from the decay back to the ground state (or another state). Because the laser frequency is adjustable, a spectrum with lots of information can be obtained. [20]

One of the strengths of collinear laser spectroscopy is its high resolution. It is therefore important to understand its nature. Collinear laser spectroscopy is performed on an accelerated beam, and the energy spread of an ion beam remains constant under acceleration. It is then possible to calculate the velocity spread using

$$\delta E = \delta\left(\frac{1}{2}mv^2\right) = mv\delta v \qquad (4.1)$$

Because the energy spread δE is constant, the velocity spread δv decreases when the velocity v is increased by an accelerating voltage of 40 to 60 kV typically. Due to the high velocity of the ions, the laser frequency observed by the beam is Doppler shifted. The small spread on the velocity leads to the high resolution of the spectroscopy technique. Instead of changing the laser frequency, it is more accurate to scan the frequency using the Doppler shift. The Doppler shift on the laser frequency in the rest frame of the moving particles allows to perform Doppler tuning: the ion velocity is changed by applying an additional acceleration voltage before the detection setup, changing the frequency in the rest frame of the ion. This way the laser frequency can be kept fixed. [35]

The Dopplerwidth of the laser beam seen by the accelerated ion beam can be written as

$$\delta\nu_D = \nu_0\frac{\delta v}{c} \qquad (4.2)$$

with ν_0 the applied laser frequency. If the total acceleration voltage is U, the velocity of the ions is $v = \sqrt{\frac{2eU}{m}}$. Implemented in equation (4.1), equation (4.2) becomes

$$\delta\nu_D = \nu_0\frac{\delta E}{\sqrt{2eUmc^2}}$$

This means that one yields a Doppler width of about 10 MHz for a beam-energy spread of about 1 eV. The resolution is therefore close to the natural line width.

All ions in the beam interact with the laser light at resonance, and thus contribute to the signal. Consequently the high resolution is achieved with the maximum possible excitation efficiency.

It is now a straightforward procedure to scan the frequency over the hyperfine structure pattern of a particular isotope, but the determination of the isotope shift is still based on a relative measurement. The outcome will be a frequency difference between two isotopes of masses m_A and $m_{A'}$, so there will also be a difference in Doppler shift. For this matter, one uses the formula for Doppler shifted frequencies (beam and laser are collinear):

$$\nu = \nu_L \frac{1 - \beta}{\sqrt{1 - \beta^2}} \tag{4.3}$$

Here ν_L is the frequency of the laser, and β is the ratio of the speed of the beam to the speed of light, given by

$$\beta = \sqrt{1 - \frac{m^2 c^4}{(eU + mc^2)^2}} \approx \sqrt{\frac{2eU}{mc^2}} \tag{4.4}$$

This means the calculation of a frequency difference between the resonances of two isotopes A and A' requires that one can calculate β_A and $\beta_{A'}$, and this is why one should know the isotope masses m_A and $m_{A'}$ and acceleration voltages U_A and $U_{A'}$ accurately.

This description can be concluded by stating that one should rely on voltage measurements and should not tune the laser frequency, but the Doppler-shifted frequency seen by the ions. This method of Doppler tuning is easier and more elegant. However, it is important to know the primary and post-acceleration voltages, masses and optical transition frequencies very accurately to fully benefit from this measurement procedure.

4.2.2 COLLAPS beam line

COLLAPS is a beam line located at ISOLDE at CERN. Its aim is the investigation of ground state properties of exotic, short lived nuclei, such as spins, nuclear moments and charge radii. It uses mainly the hyperfine interactions and isotope shifts to obtain information about nuclei. In fact, COLLAPS combines nuclear and atomic physics, as laser light is used to induce electron transitions in atoms or ions, while the goals is to know more about the ground state properties of nuclei [36]. In Figure 4.2 the floor-plan of ISOLDE is given, and COLLAPS is marked in red. In Figure 4.3 a schematic overview of the COLLAPS beam line can be found.
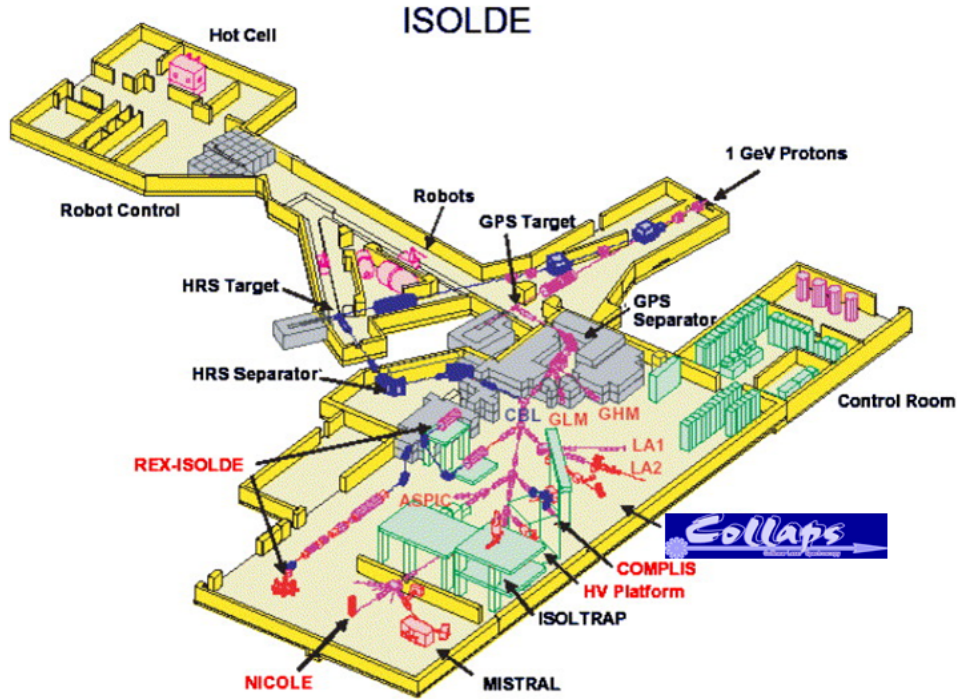
Figure 4.2: The location of the COLLAPS beam line in the ISOLDE research facility at CERN. [37]

ISCOOL

When the HRS is used, the isotopes must pass ISCOOL before entering the COLLAPS beam line. The ISCOOL (ISolde COOLer) device is a radio frequency quadrupole (RFQ) cooler and buncher, which enables trapping a certain number of ions using RF electric fields (Paul trap) [38]. It can deliver the beam as a continuous flux of particles (continuous mode), or trap ions for a certain amount of time and release the ion beam in bunches (bunched mode). The parameters which influence the accumulation and release time are the half-life of the isotopes and their yield. Depending on their chemical properties, elements can diffuse faster or slower from the target, which will influence the accumulation time. Using ISCOOL can hugely suppress the background in the laser spectroscopy measurements, as will be described in detail later. After passing ISCOOL, the ion beam enters the COLLAPS beam line.
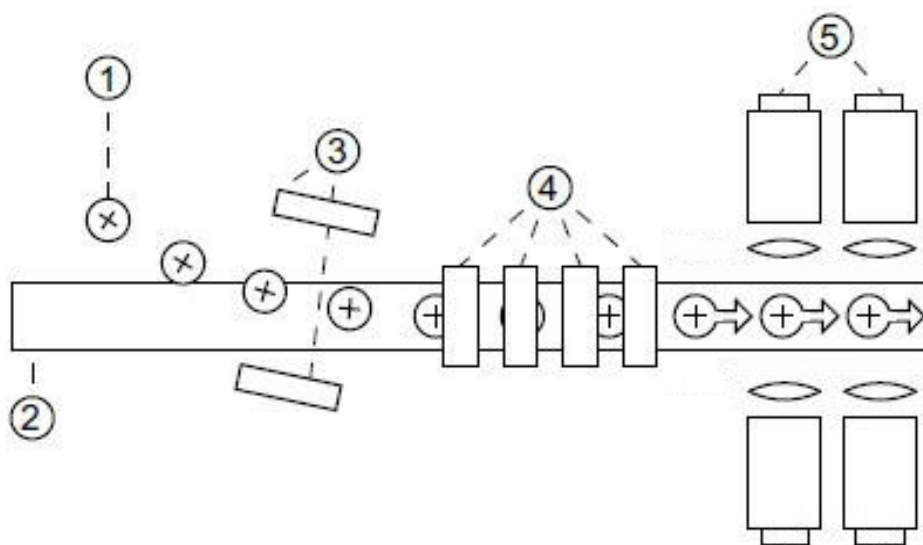
Figure 4.3: The COLLAPS beam line. The ion beam is presented in (1), (2) is the laser, (3) are the electrostatic deflectors, (4) is the post-acceleration (Doppler tuning) and (5) are the PMT's that collect the fluorescent photons. Note that in this picture, the ions are not bunched. [33]

Post-acceleration: Doppler tuning

With the electrostatic deflectors, the ion beam is superimposed collinear on a laserbeam. The beam passes a post-acceleration or retardation system. Here the Doppler tuning is done by accelerating or decelerating the beam with an electrical potential (± 10 kV). This experiment is done with ions, but in some cases it is more suitable to use atoms. In that case a charge exchange cell should be added before the detection region.

Detection with PMTs

The ions are excited by the laser if they are at resonance. When decaying back to the ground state, photons will be emitted. The photons from the fluorescent decay are collected by photomultiplier tubes (PMTs). The most important drawback of optical detection is that it might be difficult to collect and detect photons with a high efficiency, because of background noise. The main problem is the laser light that can interact and be scattered into the observation directions ($\sim 10^3$ counts/s). It might even be possible that radioactivity causes some background in the gained spectra. As the efficiency to detect a fluorescence photon is of the

order of 10^{-4}, this large background causes a significant problem. The minimum beam intensity for this detection method depends on many parameters, but depending on the complexity of the atomic spectrum one can assume limits between 10^5 and 10^7 ions/s. Nevertheless, it is possible to lower this limit by bunching the beam using the ISCOOL bunching mode, and putting a gate on the PMT signals correlated with the bunches of atoms when they pass in front of the PMT. The PMT's will then only record counts when the bunch of atoms passes in front of them. Of course therefore one has to know the time of flight of the isotopes, which is recorded by a TOF measurement at the start of the experiment (Figure 4.4). In the calcium measurements, the bunch of ions reached the PMT's in ~ 50 μs, and the gate width was 5-12 μs depending on the isotope. Because of this, the minimum intensity needed to perform an experiment is pushed down to ~ 300 ions/s, as was estimated for the measurement of ^{52}Ca.
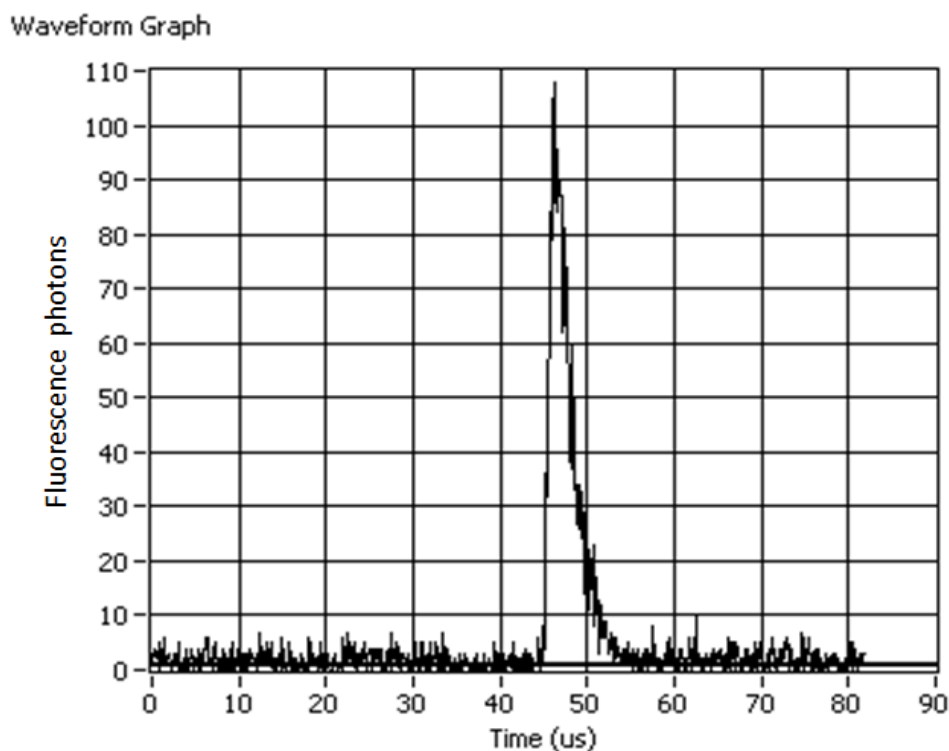
Figure 4.4: TOF (Time Of Flight) measurement for ^{40}Ca. The bunch arrives after 45 μs. The PMT's should start recording until 54 μs, which means the gate width is 9 μs.

Chapter 5

Data Analysis

This chapter consists of four parts about the data analysis. The first step in the analysis procedure is to collect all the information and summarize it to an accessible whole. Next, voltages have to be converted to frequency units so the spectra can be plotted. Both the conversion and plotting procedure are described in section 5.2. To account for an uncertainty in the ISCOOL voltage, a calibration is necessary which is explained in section 5.3. In the final section the acquirement of final numbers is elucidated.

5.1 Summary of information from experiment

There are two main sources to obtain the information that was gathered during the experiment. One is the logbook, which contains some parameters and comments about the measurement process. The other source are MCP files, which were saved using the Measurement and Control Program during the experiment. This piece of software makes it possible to monitor the experiment and save raw data. The information from both the logbook and the MCP files has to be summarized before analysis to understand the progress of the completed experiment, and to have a nice overview of all parameters that are available for the analysis.

5.1.1 Overview of the measurements

The number of saved files during the experiment are presented in Table 5.1. Such a saved file is called a run, and can start independently ('ergo') or on top of a previous file ('go') to combine statistics. In total 237 MCP files were saved, of

Isotope Number	Number of files
40	111
43	5
44	10
45	2
46	4
47	2
48	14
49	12
50	9
51	23
52	31
Kepco	14

Table 5.1: The number of MCP files per isotope that resulted from the experiment.

which 14 were calibration (Kepco) scans. The purpose of these calibration files will be explained later. Time of flight spectra were obtained in order to determine the gate width for a particular isotope. These are not included in the table.

In the next sections, only independent runs containing enough statistics which were measured in stable conditions will be taken into account. Consequently only the last file in a row of runs with combined statistics is utilized, and some other files taken when experimental conditions were unstable according to the logbook were left out completely. Table 5.2 represents the number of spectra that were used in the analysis.

5.1.2 Collecting the information

The logbook

As it was already mentioned, there are two major sources of information from the experiment: the logbook and the MCP files. The logbook contains information about the experimental conditions during a run. The most important parameters found in the logbook are the mass number of the isotope that was scanned, the IS-COOL Voltage, the laser wavelength and the gate width (in μs). It should be noted that the ISCOOL voltage was changed from 40 kV (first 80 runs) to 30 kV during the experiment, because at some point disturbingly large fluctuations worsened the results of the experiment. Furthermore, also other parameters are registered from time to time. For instance: the accumulation time of the bunching, the beam current and the laser power. Other experimental conditions or problems were de-

scribed as well. All this information was summarized in an Excel file, together with the data from the MCP files, which are described in the next paragraph.

MCP files

The data that is collected during the experiment is saved in MCP files. A typical example of such an MCP file is given in Figure 5.1. For odd Ca isotopes there are two tracks, one for the left and one for the right multiplet of the hyperfine spectrum. For even isotopes the spin is zero, we observe a single peak, and as a result there is only one track. The Prema voltage (Fluke voltage) is the post-acceleration voltage that is applied to Doppler tune the ions to a region that can then be scanned by an additional scanning voltage. There are three possible Flukes that can be adjusted, and the number of the used Fluke is also included in the MCP file. The Prema voltage is not extracted from the opened file directly, but is taken as a mean value of the voltages that were recorded during the scanning. These voltages are obtained by opening the MCP file with a simple text editor. The actual scanning is done via a line voltage and a number of counts is recorded with the PMTs as a function of the scanning voltage. It is saved per PMT, both not-gated (scaler 1 to 4) and gated (5 to 8) signals. As was described in the previous chapter, this gating improves the signal-to-noise ratio by 4 orders of magnitude. The PMTs are numbered as in Figure 5.2. Also a sum of these gated signals is given, which is called ArithScaler. In figure 5.1, this total number of counts for the gated setup is plotted against the line voltage.

5.1.3 Average laser frequency, total voltage and Kepco factor

In the analysis the laser frequency is a constant that is obtained by calculating the average of all acquired values for the frequency of the laser during the experiment. The maximum deviation from this average was 0.0002 cm^{-1}. The inverse laser frequency λ^{-1} is set to 12724.6537 cm^{-1} for the first 80 runs (40 kV) and to 12722.2985 cm^{-1} for the other runs (30 kV). By using a frequency doubler, the right laser frequency ($\nu_L = c\lambda^{-1}$) for the 4s $^2S_{1/2}$ to 4p $^2P_{3/2}$ transition is obtained. Because the laser frequency is fixed and the scanning is done via the voltage, it is important to precisely know the total voltage. It consists of three parts:

$$V_{\text{total}} = V_{\text{ISCOOL}} + V_{\text{Fluke}} + k * V_{\text{Line}} \tag{5.1}$$

The ISCOOL voltage is found in the logbook, and is approximately 40 kV for the first part, and 30 kV for the second part of the experiment. The Fluke voltage can be set at a value between −10 kV to +10 kV and is read out in the MCP
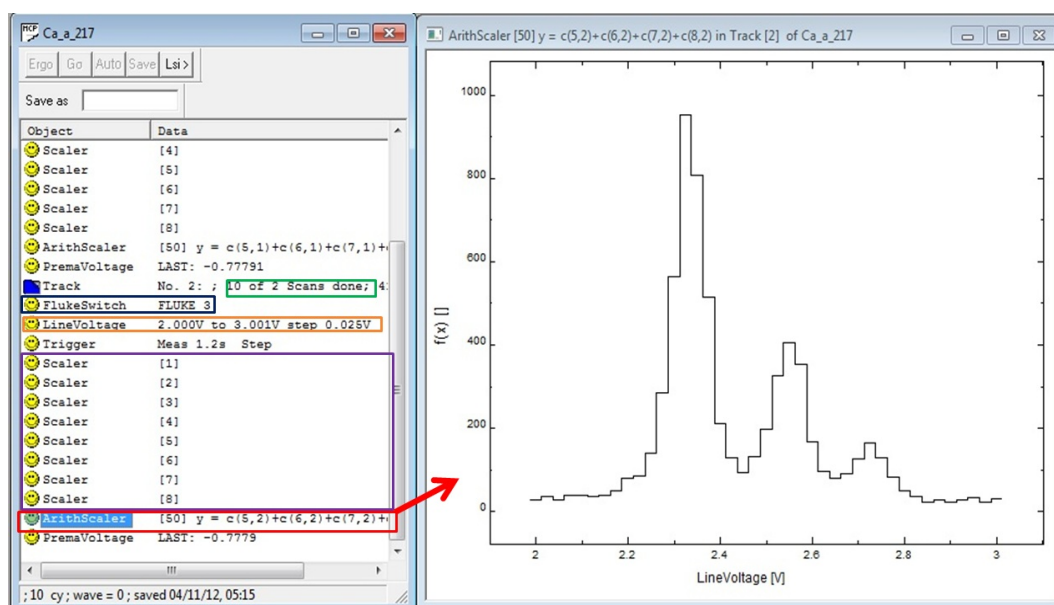
Figure 5.1: A typical MCP file. In green is the number of scans, in blue the number of the Fluke that was used, in orange there is the line voltage, in purple the different scalers (signal per PMT), and in red the total signal with a typical spectrum. In this example a spectrum of ^{47}Ca is shown (run 217, right multiplet).

file at the end of each scan. The line voltage or scanning voltage is of the order of ± 10 Volts. The latter is multiplied with an amplification factor which is called the Kepco factor (k). It can be found by a linear fit of the data in the Kepco files, where the Kepco voltage is set against the line voltage. The Kepco factor is the slope of the linear fit. The mean value of the Kepco factor is found to be 50.426(1). The fluctuations of the Kepco factor during the experiment is shown in Figure 5.3. The error of 0.001 is introduced because of the scattering of the independent Kepco determinations. This uncertainty in the Kepco factor will give rise to systematic errors, as will be discussed at the end of this chapter.

By taking into account the experimental conditions (e.g. (un)stable ISCOOL voltage, possible laser jumps) a selection of runs can be obtained. It is important that right before or right after a run, a reference run (^{40}Ca) was executed with the same experimental conditions. As will be clarified in the next sections, this is crucial to calculate the isotope shifts. In Table 5.2 the number files per isotope that are selected for the data analysis are summarized. It should be noted however that the biggest difference with Table 5.1 is that some files were saved on top of another file. To get independent measurement runs, only the last saved file of such chains is used, or previous files are subtracted to reduce the statistics when necessary. This last remark will also be elucidated in the next section.
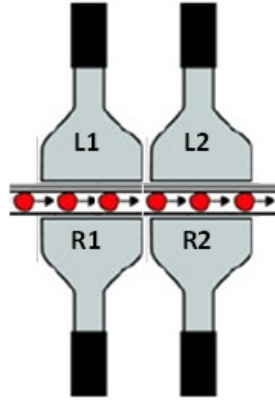
Figure 5.2: The numbering of the PMTs as saved in the MCP file. L stands for left, R stands for right, the front detectors relative to the incoming beam are numbered 1, the rear detectors are numbered 2. In the MCP file, L1 corresponds to scaler 1 and 5, L2 to 2 and 6, R1 to 3 and 7 and R2 to 4 and 8 for ungated and gated signals respectively.

5.2 Analysis procedure

5.2.1 Conversion of voltages to frequencies

As was mentioned in equation (5.1), the ISCOOl voltage, Fluke voltage and scanning voltage are used to calculate the total voltage. This voltage can be converted to a frequency by using formula (4.3) and (4.4), which were applied in a code written in C++. The masses used in this formula have to be the singly ionized masses of the Ca isotopes. This means the mass is calculated

$$m_{\text{ion}} = m_{\text{atom}} - m_{\text{electron}} + m_{\text{ionization energy}}$$

The electron mass is $0.000548580u$ [39], the first ionization energy of Ca is 6.11316 eV [40], which can be converted to atomic mass units with $E = mc^2$ to be $\sim 7*10^{-9}$ u. The atomic masses and calculated ion masses are given in Table 5.3. After the conversion counts are given in function of frequencies.

5.2.2 Fitting procedure

The next step concerns the fitting of the data points, which are a number of counts for a certain frequency. The number of peaks in a fit depends on the spin. An example of a spectrum of ^{47}Ca together with its transition scheme is given in

Isotope	# files (40 kV)	# files (30 kV)	Spin
43	-	3	7/2
44	3	4	0
45	-	2	7/2
46	-	2	0
47	-	2	7/2
48	4	5	0
49	4	4	3/2
50	1	3	0
51	-	3	(3/2)
52	5	4	0

Table 5.2: The number of MCP files per isotope that were used in the analysis, with ISCOOL voltage 40 and 30 keV respectively. Every file is accompanied by a ^{40}Ca reference file. In the last column, the spins are shown. For ^{51}Ca, the spin is yet to be observed experimentally, but from theory it is believed to be 3/2 [3]. This will need verification.

Isotope	Atomic mass (u)	Ion mass (u)
40	39.962590863(22) [41]	39.96204229(22)
43	42.95876634(24) [41]	42.95821777(24)
44	43.95548135(34) [41]	43.95493277(34)
45	44.95618614(39) [41]	44.95563757(39)
46	45.9536873(24) [41]	45.9531387(24)
47	46.9545407(24) [41]	46.9539922(24)
48	47.9525241(23) [41]	47.9519756(23)
49	48.9556641(23) [41]	48.9551155(23)
50	49.9575004(37) [41]	49.9569518(37)
51	50.96098859(39) [42]	50.96044002(39)
52	51.96323691(37) [42]	51.96268834(37)

Table 5.3: Atom masses and calculated ion masses for all used Ca isotopes. References of the atomic masses are given in square brackets.
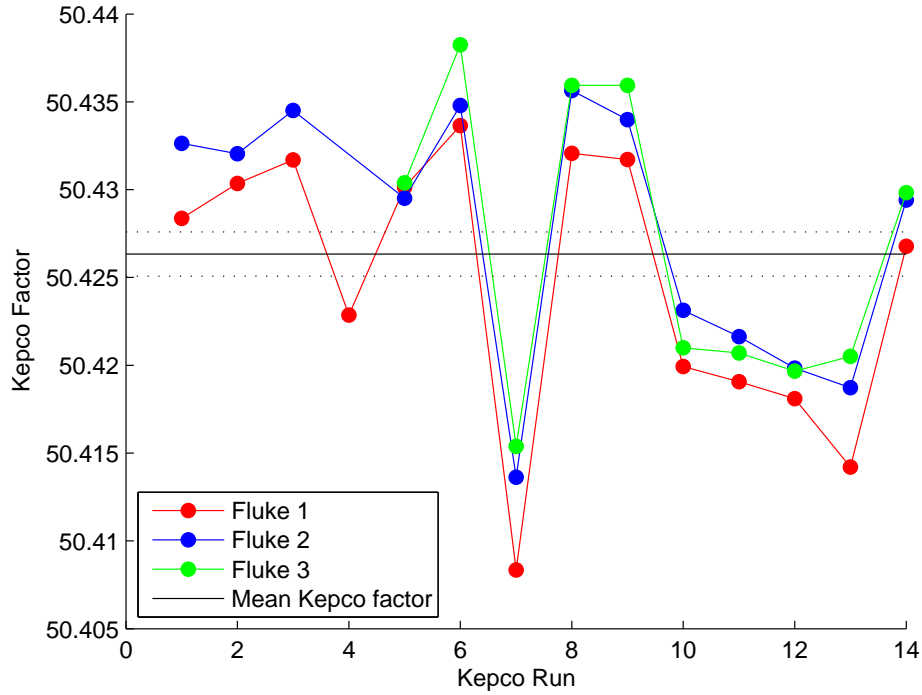
Figure 5.3: The Kepco factor obtained from the 14 Kepco scans during the experiment. The dashed lines are the mean Kepco factors for every Fluke, and the total mean Kepco factor is given by the black line which is calculated to be 50.426(1). The error on the individual Kepco values is of the order of 0.0001.

Figure 5.4. The ionic transition measured was the 4s $^2P_{1/2}$ to 4p $^2P_{3/2}$ transition. Therefore the position of the ith peak should be calculated as

$$\nu_i = C_1 A(^2S_{1/2}) + C_2 A(^2P_{3/2}) + C_3 B(^2P_{3/2}) + \nu_0 \tag{5.2}$$

Here $A(^2S_{1/2})$ is the A parameter for the $^2S_{1/2}$ ionic state and $A(^2P_{3/2})$ and $B(^2P_{3/2})$ are the A and B parameters for the $^2P_{3/2}$ ionic state respectively. The C_i factors can be calculated from equations (3.15), (3.17) and (3.18). There is no B factor for the $^2S_{1/2}$ state, because for this state $J < 1$. ν_0 is the fitted transition frequency of the $^2S_{1/2}$ to $^2P_{3/2}$ transition, and is called the center of gravity of the hyperfine structure. The difference in the center of gravity of an isotope and the reference isotope ^{40}Ca is the isotope shift. The fitting is done with a Voigt profile with a common line width for all peaks.

The center of gravity shifts the spectrum, and thus determines the placement of
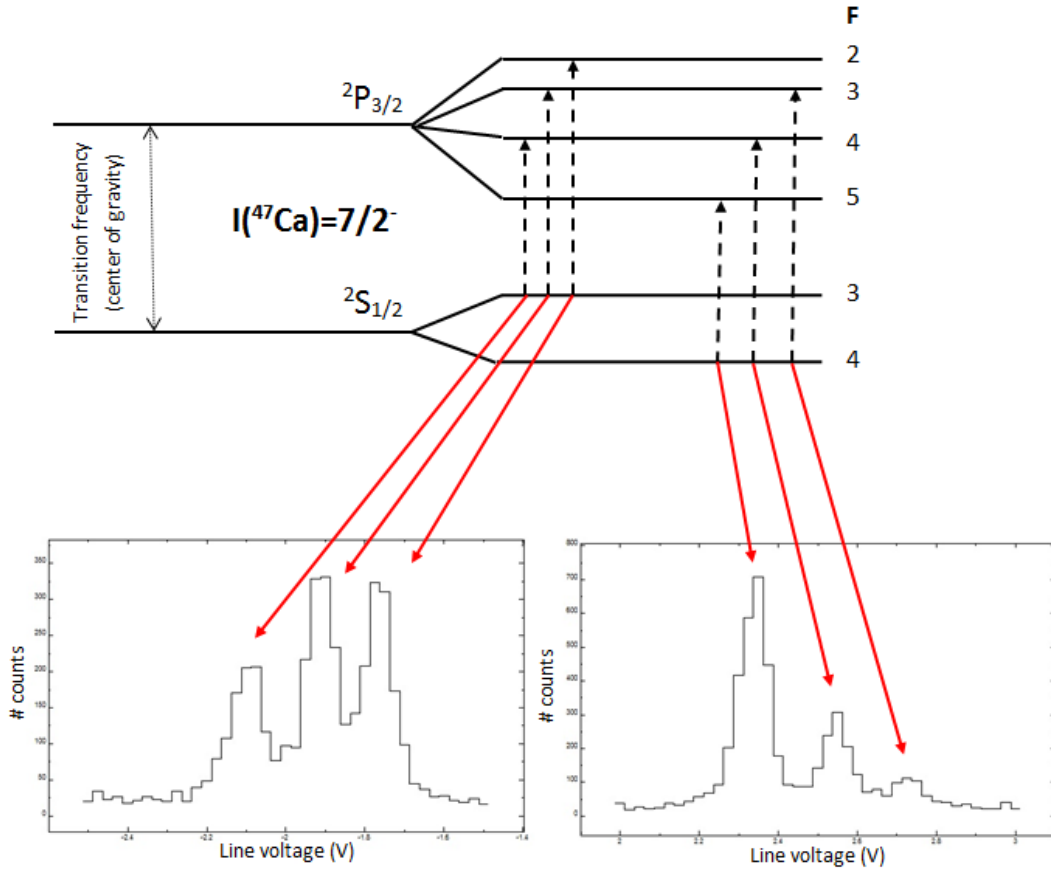
Figure 5.4: The transition scheme of ^{47}Ca, together with the left and right multiplet from the MCP file. The red arrows connects the transitions with the peaks in the spectrum. The total angular momentum and its selection rules have to be used as in equations (3.13) and (3.14). From the relative peak positions the A- and B-factors can be calculated with formula (3.19)

the spectrum. The A and B factors establish the relative peak positions. Other parameters are the background, the peak intensity and the peak width (Lorentzian and Gaussian). By minimizing the difference in the fit and the experimental values, the parameters and their errors are obtained. This can be done by minimizing the χ^2 value:

$$\chi^2 = \sum_{i=1}^{N} \frac{(y_{\text{exp},i} - y_{\text{fit},i})^2}{\sigma_{\text{exp},i}^2} \tag{5.3}$$

The numerator is the difference between fitted and experimental values, and the denominator is the uncertainty on the experimental number of counts which is

given by the square root of the number of counts $\sigma_{\text{exp},i} = \sqrt{y_{\text{exp},i}}$. The code for the fitting was written in a ROOT script based on the standard MINUIT fitting package. Nevertheless, the spectrum should always be checked visually and the fitted parameters have to take reasonable start values to obtain a converging fit. One should notice that all the parameters can be left free, or some of them can be fixed to a certain value to reduce the degrees of freedom. For the ^{47}Ca, run 217 the fitted spectrum (both multiplets) is given in Figure 5.5.
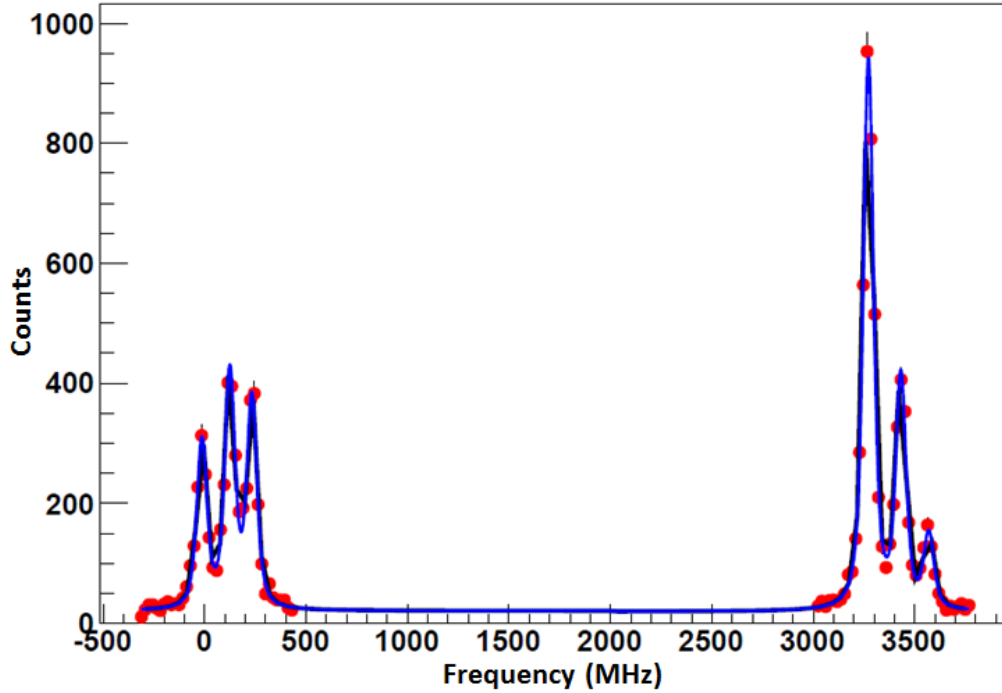
Figure 5.5: The fitted spectrum of ^{47}Ca, run 217, both multiplets. As ^{47}Ca has spin 7/2, the hyperfine spectrum has six peaks. From the fit one can obtain the center of gravity, A and B-factors and peak width.

5.2.3 Weighted mean and errors

In this section, the formulas for the weighted mean and the errors on the fitting parameters and mean values are presented [43]. The fitting parameters come with uncertainties $\sigma_{\text{fit},i}$. Because of imperfections in the fit, which are exposed by means of χ^2, the uncertainties are multiplied with the square root of the reduced χ^2:

$$\sigma_i = \sigma_{\text{fit},i} \sqrt{\chi^2_{\text{red}}} \tag{5.4}$$

Where χ^2_{red} is calculated as

$$\chi^2_{\text{red}} = \frac{1}{n} \sum_{i=1}^{N} \frac{(y_{\text{exp},i} - y_{\text{fit},i})^2}{\sigma^2_{\text{exp},i}}$$

With n the degree of freedom, which is the number of points in the spectrum minus the number of fit parameters. As could be seen from Table 5.2, there are multiple independent runs per isotope. This implicates there are multiple spectra, and the mean of the obtained experimental values can be calculated using the formula for the weighted mean:

$$\mu = \frac{\sum_{i=1}^{N} \frac{x_i}{\sigma_i^2}}{\sum_{i=1}^{N} \frac{1}{\sigma_i^2}} \tag{5.5}$$

The error on the mean value is the maximum of two errors, the statistical and the scattering error:

$$\sigma^2_{\text{stat}} = \frac{1}{\sum_{i=1}^{N} \frac{1}{\sigma_i^2}} \tag{5.6}$$

$$\sigma^2_{\text{scatter}} = \frac{1}{(N-1) \sum_{i=1}^{N} \frac{1}{\sigma_i^2}} \sum_{i=1}^{N} \frac{1}{\sigma_i^2} (x_i - \mu)^2 \tag{5.7}$$

Were N is the number of independent measurements for the same isotope. In general, there is a systematic error which should be added quadratically to this value to get the total error. This systematic error will be discussed at the end of the chapter.

5.2.4 High statistics problems

A problem that was encountered during the analysis is that for some runs with high counts on spin zero isotopes (one peak), χ^2_{red} was higher than one would expect. Instead of a value close to one, ranging up to 2.5, in some cases χ^2_{red} was more than 5. This unexpected χ^2_{red} value means the fit is not good, and consequently the center of gravity of the spectrum might be shifted. First we discuss if the center of gravity changes significantly when statistics are lowered by splitting files. Afterward a possible source of this high χ^2_{red} is discussed, including a compensation of this effect.

High number of counts

The problem with a high χ^2_{red} is only present with spin zero isotopes and only when a high number of counts is reached, as in Figure 5.6. To investigate if the fitted center of gravity is consistent within error bars, the statistics are reduced by subtracting previous saved files if possible, and by splitting the measurement in 2 front and 2 back detectors instead of 4 detectors at once. All files are then fitted independently. In Table 5.4 the results of such an analysis are given. It is clear that in general the center of gravity, which is for our experiment the most important value, does not change significantly. In other words, although χ^2_{red} is lowered, this has no influence on the parameters. It is thus acceptable to use the files, despite the high χ^2_{red} value.
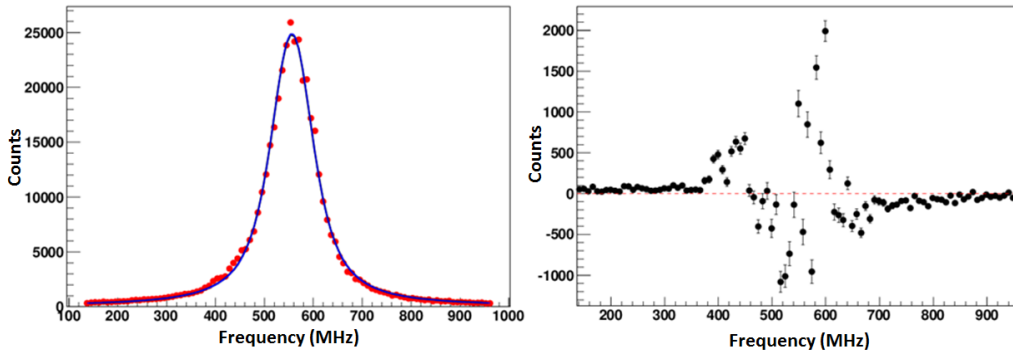
Figure 5.6: On the left the fitted spectrum of ^{40}Ca, run 17, can be seen. On the right side the residuals plot, the difference between the fit and the experimental points for every point including the error, is given. $\chi^2_{red} = 20.1$ ($n = 95$), due to the relatively small errors in the peak.

The line shape

The χ^2_{red} depends on how well the fitted Voigt profile matches the experimental points, including the errors. A high χ^2_{red} thus implies that the shape of the Voigt profile does not fit the experimental points well. As the error on the number of counts is the square root of this number, it is relatively small with a high number of counts. This means the fitting becomes very sensitive to the used line shape. Since such a high χ^2_{red} is obtained, a Voigt profile is possibly not the right line shape to fit the experimental data. Therefore all fit parameters are multiplied with $\sqrt{\chi^2_{red}}$, as was pointed out in equation (5.4). By doing this, the deviation of the fit with a Voigt profile is accounted for.

Isotope	Run	Centroid	Lorentz	Gauss	χ^2_{red}
40	17	556.1(1)	20.6(4)	192.4(1.2)	20.1
	17 front	557.0(1)	21.9(5)	165.8(1.6)	12.5
	17 rear	555.4(1)	20.3(6)	211.0(1.9)	9.6
	average	556.2(1)	21.1(4)	188.4(1.2)	-
40	158	611.7(3)	17.4(12)	144.3(4.5)	10.5
	158 front	611.0(5)	17.4(16)	129.7(5.9)	6.3
	158 rear	613.0(7)	18.7(26)	150.7(9.9)	3.6
	average	612.0(4)	18.1(14)	140.3(5.2)	-
44	20	1396.3(2)	20.7(4)	110.2(1.9)	8.4
	20 front	1397.2(2)	20.0(6)	98.7(2.6)	5.6
	20 rear	1395.6(2)	21.4(4)	117.5(9)	4.4
	average	1396.4(2)	20.7(3)	108.1(9)	-
48	160	2306.0(2)	22.2(6)	115.6(2.4)	5.1
	160-159 front	2305.5(4)	23.4(10)	100.8(4.5)	5.5
	160-159 rear	2306.5(4)	22.0(13)	121.0(5.4)	3.4
	average	2306.0(3)	22.7(8)	110.9(3.5)	-

Table 5.4: Center of gravity, Lorentz and Gauss widths, and χ^2_{red} for 4 different runs of 3 isotopes. In the first row the original spectrum was used, the next rows are the spectra for the front and rear detectors respectively, and if possible a previous saved file is subtracted. In the last row of every segment the average of the values for the two rows of detectors is calculated. When the fourth row is compared with the first row of every segment, it is clear that the values do not change significantly. Note that the errors on the parameters are the fit errors, and should be multiplied with $\sqrt{\chi^2_{\text{red}}}$.

5.3 ISCOOL calibration

One of the terms in formula (5.1) to obtain the total voltage is the ISCOOL voltage. Because of an uncertainty of 0.2% on the ISCOOL voltage read-out, a calibration is necessary [44]. This is done by comparing the experimental isotope shifts with the values from literature, and changing the ISCOOL voltage until our measured isotope shifts are consistent with those from literature. The calibration should be accurate up to at least 1 V in order to limit the frequency error on the isotope shift.

The literature values that were used are from earlier collinear laser spectroscopy experiments by Vermeeren *et al.* [45] and Mårtensson-Pendrill *et al.* [46]. These values are from the 4s $^2S_{1/2}$ to 4p $^2P_{1/2}$ transition, but Silverans *et al.* proved that

Isotope	$\delta\nu_{\text{lit}}$ (MHz)
40	0
43	672(12)
44	842(9)
45	1287(10)
46	1696(10)
48	1091(13)
50	1951(17)

Table 5.5: Literature values of the isotope shift, recalculated so ^{40}Ca is the reference isotope [45, 46]. A quoted systematic calibration error of 2 MHz per mass unit difference is accounted for.

the isotope shift is independent of J [47]. Therefore these values can also be used for the 4s $^2S_{1/2}$ to 4p $^2P_{3/2}$ transition. Because in the previous experiment the reference isotope was the ^{44}Ca isotope, the isotope shifts have to be recalculated relative to ^{40}Ca first. In Table 5.5 the literature values are given relative to ^{40}Ca. As was quoted in the articles of Vermeeren and Mårtensson-Pendrill, a systematic calibration error of 2 MHz per mass unit difference is added quadratically to the statistical error.

Different calibrations were carried out, ranging from 0V up to -16V. By minimizing the χ^2 value of the difference in isotope shift between literature and experiment, the obtained calibration values to correct the ISCOOL voltage are -15.7(1.2) V for 40 kV, and -12.91(65) V for 30 kV (Figure 5.7). For convenience, -15.5 V and -13 V were used in further analysis. In Figure 5.8 the difference in literature and experimental isotope shift for both 40 kV and 30 kV are shown before and after the calibration.
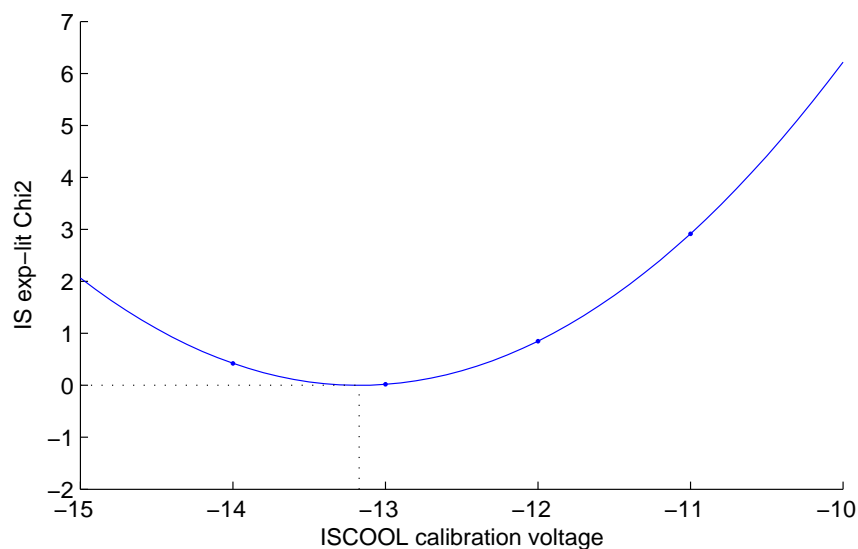
Figure 5.7: Minimizing the χ^2 value of the difference in isotope shift between literature and experiment for 30 kV ISCOOL voltage. The minimum is found to be at 12.91(65) V.
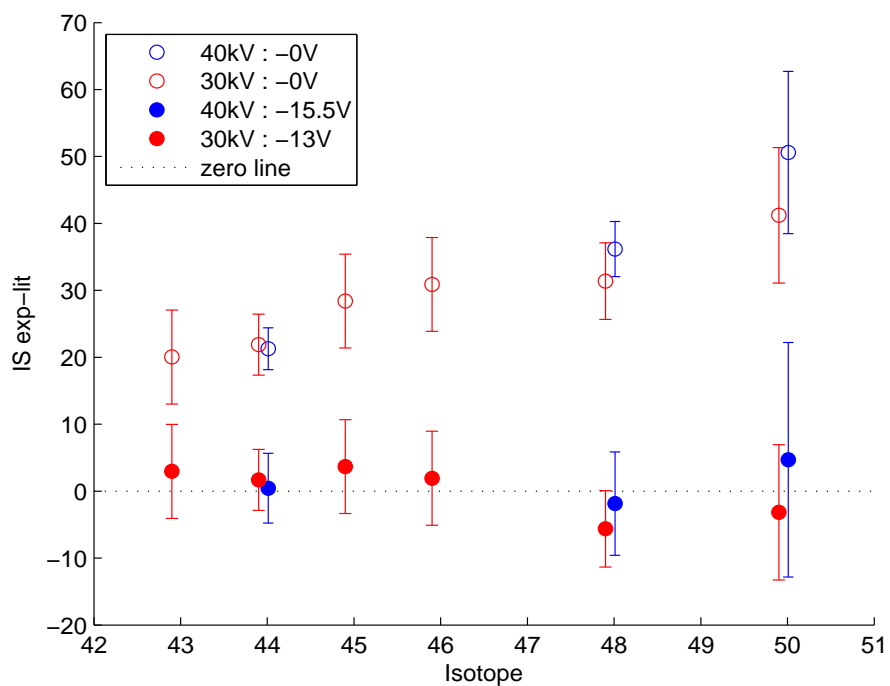
Figure 5.8: The difference in isotope shifts from literature and experiment for 40 kV and 30 kV, before and after calibration, for every isotope. It is clear that the calibration leads to a serious improvement concerning the isotope shift.

5.4 Obtaining final values

5.4.1 Isotope shifts, differences in mean square charge radii and nuclear moments

As the ISCOOL voltage is now calibrated, the voltages have to be corrected and converted to frequencies once more. The spectra can be fitted again and the final values for the fitting parameters can be found. The isotope shifts can be calculated using (3.6), and the difference in mean square charge radii can be deduced from equations (3.7), (3.8) and (3.11):

$$\delta\nu^{A,A'} = \frac{m_{A'} - m_A}{m_A(m_{A'} + m_e)}(K_{\text{NMS}} + K_{\text{SMS}}) + F\delta\langle r^2\rangle^{A,A'}$$

This can be rewritten to an expression for the difference in mean square charge radius:

$$\delta\langle r^2\rangle^{A,A'} = \frac{\delta\nu^{A,A'} - \frac{m_{A'} - m_A}{m_A(m_{A'} + m_e)}(K_{\text{NMS}} + K_{\text{SMS}})}{F} \tag{5.8}$$

The moments can be calculated using the hyperfine A and B parameters together with (3.20) and (3.21). Therefore, a trustworthy reference value is needed from literature. Note that the reference isotope for calculating the moments need not to be the same as the reference isotope for the isotope shift. The reference isotope for the moments will be ^{43}Ca as this is the only stable odd calcium isotope, and is investigated most in past experiments. In the next chapter, these final results are summarized and discussed in terms of the motivation.

5.4.2 Systematic errors

On top of the error from the fit, which was defined as the maximum between the statistical and scattering error, a systematic error should be added quadratically. The systematic error is due to the uncertainties in the parameters that are used when converting the voltages into frequencies. Consequently, next errors should be taken into account:

- The laser wavelength

- The mass of the isotope

- The Kepco factor

- The ISCOOL calibration voltage

In this work these parameters will be treated independently and the systematic error will only be estimated, as a profound discussion is complex due to possible correlations between these parameters.

Due to equations (4.3) and (4.4), the uncertainties on these parameters give rise to a mass dependent error. This means that for every final value (e.g. the isotope shift and the hyperfine parameters) the influence for every of these four parameters has to be estimated for every isotope. To estimate the systematic error due to a certain parameter, the error on this parameter was added (or subtracted) from the mean value that was used in the first place and the voltages were reconverted to frequencies. Afterward, the spectra was fitted again and final values were recalculated. The difference between the original final value and the newly obtained final value is then accepted as the systematic error on the final value for a certain isotope due to a particular parameter. These values are added quadratically to get a value for all parameters together. To improve the clarity of the text, these isotope dependent values were recalculated to mass dependent values relative to the reference isotope. Therefore, the maximum value per unit mass (in u) was used. This means that for example the systematic error on ^{43}Ca is roughly 3 times the systematic error per unit mass if ^{40}Ca was the reference isotope, and systematic errors increase with the mass number. In the next chapter, the most important contributions to the systematic errors are described for isotope shifts, differences in charge radii and hyperfine parameters, and a estimation following previous procedure will be given.

Chapter 6

Results and Discussion

In this chapter the results are presented and discussed. In the first section the final numbers for the isotope shifts and differences in mean square charge radii are given and compared to the values found in literature. In this analysis, the spin of ^{51}Ca is assumed to be 3/2. In the second part this spin is confirmed experimentally and final hyperfine parameters are presented. In the last section the nuclear moments are calculated using these hyperfine parameters together with some literature values. The experimental nuclear moments are compared to literature values and discussed in the framework of shell model calculations, to gain insight in the composition of the wave function of the ground state of Ca isotopes.

6.1 Isotope shifts and differences in mean square charge radii

In section 5.3 the known isotope shifts were used to calibrate the ISCOOL voltage. Now it is possible to determine final numbers for the isotope shifts from our experiment. Using formula (5.8) it is then possible to calculate differences in mean square charge radii. First our results are compared to literature values, and consequently differences in mean square charge radii are determined using F and K_{SMS} from literature. In the second part of this section the mean square charge radii are determined more precisely using own experimentally obtained factors. Subsequently the systematical errors will be estimated and the results will be discussed in terms of shell closures.

6.1.1 Comparison to literature

To be able to compare isotope shifts to literature, the experimental isotope shifts were recalculated relative to ^{44}Ca. The final numbers for the isotope shift can be found in Table 6.1. Only statistical errors are taken into account. The mean square charge radii are calculated from the isotope shifts, and are thus given as a difference in mean square charge radius rather than an absolute value. In order to obtain $\delta\langle r^2\rangle^{A,A'}$, formula (5.8) is used with $F = -283(6)$ MHz/fm^2 and $K_{\text{SMS}} = -9.2(3.8)$ GHz u [46]. The ion masses from table 5.3 are used, but are corrected for 19 electrons as we are dealing with a nuclear mass instead of an ion mass now. K_{NMS} can be calculated with equation (3.9), with $\nu_0^A = \nu_0^{40} = 761904700$ MHz [48].
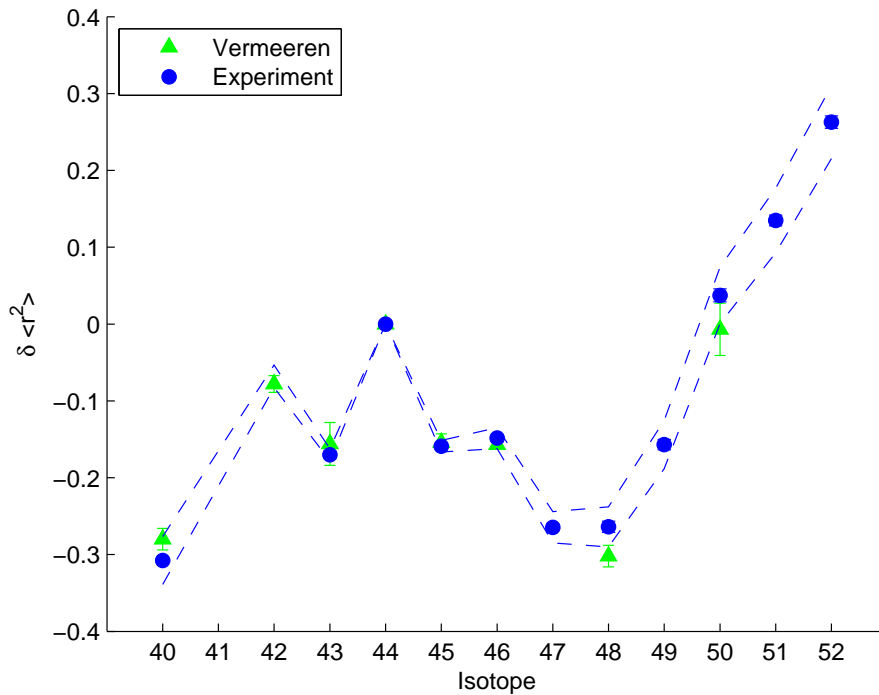
Figure 6.1: Differences in mean square charge radii obtained from this experiment and by Vermeeren *et al.* [45] relative to ^{44}Ca. The error bars on the experimental data are mainly due to the uncertainties in the isotope shift. The errors deduced from uncertainties in F and K_{SMS} are given with a blue dashed line.

In Figure 6.1 the literature and experimental values of the differences in mean square charge radii are plotted for all measured isotopes, relative to ^{44}Ca. A very

Isotope	$\delta\nu_{\mathbf{exp}}$ (MHz)	$\delta\nu_{S_{1/2}\to P_{1/2}}$ (MHz) [45]	$\delta\nu_{S_{1/2}\to P_{3/2}}$ (MHz) [46]
40	-842.6(8)	-842(3)	-842(13)
43	-167.7(1.2)	-170(8)	-165(14)
44	0(1.2)	0	0
45	252.1(1.1)	249(3)	-
46	446.6(1.1)	445.2(6)	450(13)
47	669.1(1.2)	-	-
48	850.2(2.0)	854(3)	857(14)
49	994.7(1.9)	-	-
50	1107.2(2.4)	1109(9)	-
51	1240.9(2.0)	-	-
52	1359.4(2.3)	-	-

Table 6.1: Comparison between literature and experimental values for the isotope shift, relative to ^{44}Ca as a reference. Note that in our experiment, the 4s $^2S_{1/2}$ to 4p $^2P_{3/2}$ transition was used. Nevertheless, the isotope shift should be independent of J [47]. Systematic errors are not included in this table.

Isotope	$\delta\langle r^2\rangle$ (fm^2)	$\delta\langle r^2\rangle$ (fm^2) [45]
40	-0.308(3)(31)	-0.280(14)(31)
41	-	-
42	-	-0.078(11)(15)
43	-0.170(4)(8)	-0.156(28)(8)
44	0.000(4)	0
45	-0.159(4)(8)	-0.154(11)(8)
46	-0.148(4)(14)	-0.157(5)(14)
47	-0.265(4)(20)	-
48	-0.264(7)(26)	-0.302(14)(26)
49	-0.157(7)(31)	-
50	0.037(8)(37)	-0.007(34)(37)
51	0.135(7)(42)	-
52	0.263(8)(47)	-

Table 6.2: Differences in mean square charge radii compared to the results of Vermeeren *et al.* [45] with ^{44}Ca as the reference. The differences in charge radii are all calculated with the same F and K_{SMS} from literature [46]. The first error is mainly due to the errors on the isotope shifts. The second error is due to the electronic factor F and the specific mass shift constant K_{SMS}. Systematic errors are not included.

good agreement with literature values is found. All experimental and literature values are summarized in Table 6.2. Note that only the literature values that were calculated with the same F and K_{SMS} are included in the table. The mean square charge radii for $^{49,51,52}\text{Ca}$ were measured for the first time.

6.1.2 Determination of mean square charge radii with a higher precision

In the previous discussion the field shift factor F and the specific mass shift factor K_{SMS} were obtained from literature. It is also possible, however, to deduce these factors from our experimental values. This is can be done with a King plot, in the same way as the F and K_{SMS} values from Mårtensson-Pendrill *et al.* [46] mentioned above were deduced. Therefore equation (5.8) needs to be rewritten, using the experimental isotope shifts from this work, and the difference in mean square charge radii from Palmer *et al.* [49]. Palmer's group used three sets of optical data [50, 51, 52] in conjunction with a combined analysis of muonic-atom isotope shifts and electron scattering data [53] to derive improved values for differences in charge radii. The formula used to obtain F and K_{SMS} is:

$$\frac{\delta\nu_{\text{exp}}^{A,A'}}{B} - K_{\text{NMS}} = F\frac{\delta\langle r^2\rangle_{\text{lit}}^{A,A'}}{B} + K_{\text{SMS}}$$

with

$$B = \frac{m_{A'} - m_A}{m_A(m_{A'} + m_e)}$$

Here K_{NMS} is calculated as in equation (3.9). The King plot containing the isotope shifts of our experiment, and the differences in mean square charge radii from Palmer's group can be found in Figure 6.2. This plot corresponds to a linear relationship, as was expected from the formula above.

The slope of the linear plot in Figure 6.2 is the field shift factor F, and the intersection with the vertical axis is equal to K_{SMS}. It was determined that $F_{\text{exp}} = -284(4)$ MHz/fm^2 and $K_{\text{SMS, exp}} = -12.1(7)$ GHz u, which is in agreement within the error bars with the literature values [46], as can be seen in Table 6.3. However, due to the more accurate isotope shifts, both values are obtained with a higher precision than in Mårtensson-Pendrill's work.

Since F and K_{SMS} are now determined from our data, it is possible to recalculate the differences of the mean square charge radii with these newly obtained numbers. The calculation method of the mean square charge radii is exactly the same as before. To show that the charge radii are now shifted, the values for the difference
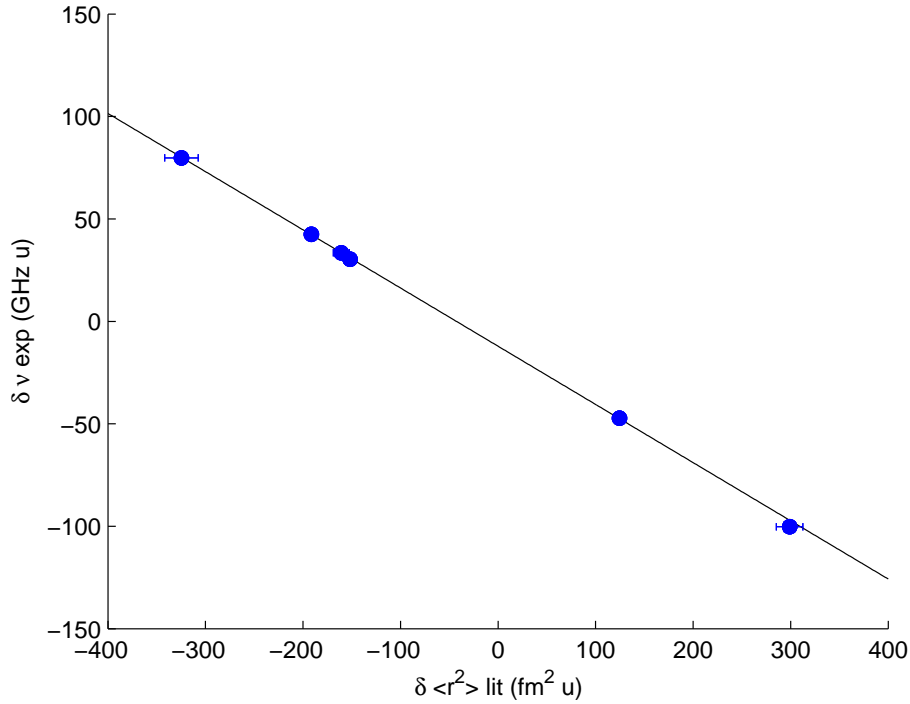
Figure 6.2: King plot where the experimental isotope shifts from this work are combined with the charge radii from Palmer *et al.* [49]. This was done to obtain an experimental F_{exp} and $K_{\text{SMS, exp}}$, similar to the work of Mårtensson-Pendrill *et al.* [46]. The fitting and acquiring of the slope and intercept was done with the method of York *et al.* [54].

in mean square charge radii calculated with both electronic factors and specific mass shift constants are plotted in Figure 6.3, relative to ^{40}Ca. All values are in agreement inside error bars due to the uncertainties in F and K_{SMS}. Note that using a different F changes the slope, and a different K_{SMS} causes a shift in the dots. This can also be seen from equation (5.8). Final numbers for isotope shifts and differences in mean square charge radii relative to ^{40}Ca can be found in Table 6.4.

	Literature [46]	Experiment
F	-283(6) MHz/fm	-284(4) MHz/fm
K$_{\text{SMS}}$	-9.2(3.8) GHz u	-12.1(7) GHz u

Table 6.3: Comparison of experimentally determined electronic factor F and specific mass shift constant K_{SMS} with literature values.

Isotope	$\delta\nu$ (MHz)	$\delta\langle r^2\rangle$ (fm^2)	$\delta\langle r^2\rangle_{\text{recalc}}$ (fm^2)
43	674.9(9)	0.138(3)(24)	0.119(3)(4)
44	842.6(8)	0.308(3)(31)	0.283(3)(7)
45	1094.7(8)	0.149(3)(37)	0.120(3)(7)
46	1289.2(8)	0.159(3)(44)	0.125(3)(8)
47	1511.7(9)	0.043(3)(50)	0.005(3)(9)
48	1692.8(1.9)	0.044(7)(56)	0.001(7)(10)
49	1837.3(1.7)	0.151(6)(62)	0.103(6)(11)
50	1949.8(2.2)	0.345(8)(68)	0.292(8)(12)
51	2083.4(1.8)	0.443(7)(73)	0.385(7)(14)
52	2202.0(2.1)	0.570(8)(79)	0.509(8)(15)

Table 6.4: Final isotope shifts and differences in mean square charge radii relative to ^{40}Ca. On the difference in mean square charge radii, the first error bar is due to the isotope shift. The second error is due to the electronic factor F and the specific mass shift constant K_{SMS}. The last column are the recalculated mean square charge radii with F and K_{SMS} deduced from the King plot. Systematic errors are not included, but can be estimated as was described in the text to be ~ 0.4 MHz/u for the isotope shift and ~ 0.001 fm^2/u for the differences in mean square charge radii.
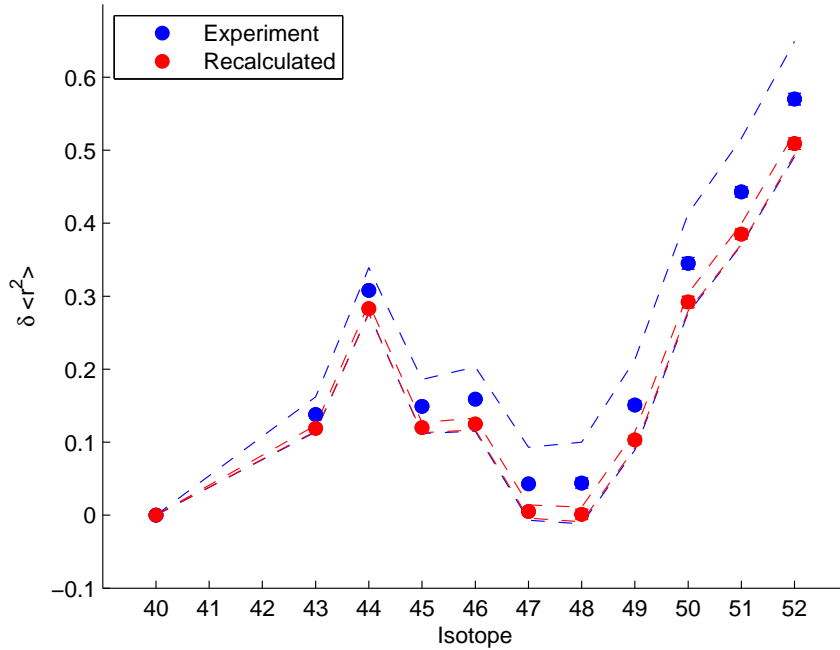
Figure 6.3: The previously calculated differences in mean square charge radii using the field shift factor and specific mass shift factor from [46] (blue), and the recalculated mean square charge radii using F and K_{SMS} obtained from the King plot (red), relative to ^{40}Ca. The error bars on the experimental data are purely deduced from uncertainties in the isotope shift. The errors due to uncertainties in F and K_{SMS} are given with a dashed line.

6.1.3   Estimation of systematic errors

The systematic errors were estimated as described in section 5.4.2. The systematic error due to the error on the mean Kepco factor is estimated to be less than 0.01 MHz for every isotope. The laser frequency and mass cause errors that are maximum 0.1 MHz. Therefore, the systematic error is dominated by the error on the ISCOOL calibration voltage, which is 0.65 V for 30 kV and 1.2 V for 40 kV. This causes a maximal error of 0.26 MHz/u and 0.40 MHz/u on 30 and 40 kV respectively. Because some isotopes are measured with both ISCOOL voltages, and it is preferred to combine the results, the estimated systematical error is taken 0.4 MHz/u. When these errors are added quadratically to the statistical errors and the errors on charge radii are recalculated, an extra systematic error of maximum 0.001 fm^2/u can be estimated.

6.1.4   Discussion concerning shell closures

With this information on the charge radii of calcium, it is possible to extend our knowledge in terms of the (sub-)shell closures in exotic nuclei in this region. When looking at the neutron number, it is already known that $N = 20$ and $N = 28$ are magic numbers. As was pointed out in Chapter 2, it is interesting to investigate if such a shell gap can also be found at $N = 32$. It is established by Angeli *et al.* [55] that a shell gap is presented in most cases by a change of slope in the sequence of mean square charge radii. When looking at $N = 28$, $N = 50$ or $N = 82$ for example (Figure 2.3 and Figure 6.4), it is clear that the trend of charge radii flattens out before suddenly ascending after the shell closure. For a reason that is still not truly understood this trend can not be seen with $N = 20$. Here the charge radius varies smoothly and without a bend across the shell gap [56, 57, 58].
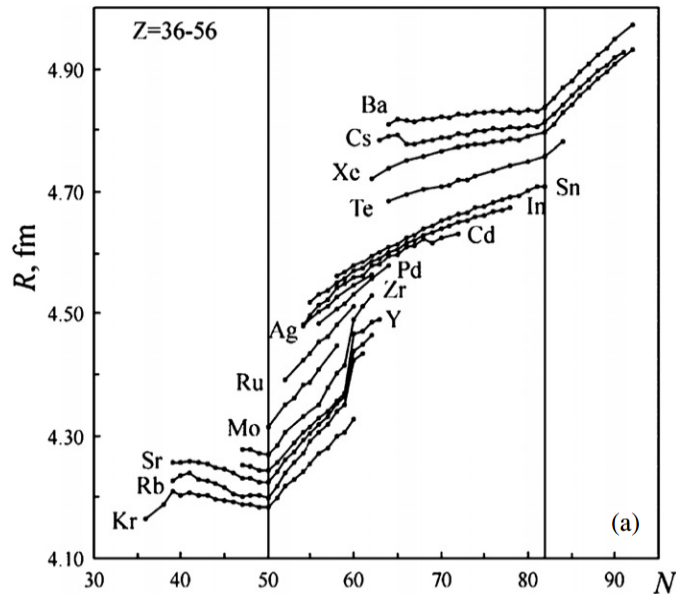
Figure 6.4: The root mean square charge radius $\langle r^2 \rangle^{1/2}$ for the isotopes in the vicinity of $N = 50, 82$ [55].

Since the differences in mean square charge radii of calcium isotopes are now fully determined, we can update Figure 2.3. For this the recalculated values of our experiment, updated values for the K experiment [59] and literature on other elements [60, 61] were used, resulting in Figure 6.5. When the $N = 28$ shell closure is approached, the charge radii tend to stagnate. Right after $N = 28$ a steep increase can be observed. A similar effect would be expected for $N = 32$ if this

would also represent a shell gap. It is clear from Figure 6.5 that such a stagnating effect is not observed for $N = 32$. Therefore the charge radii do not supply us with any evidence for such a shell closure. Nevertheless, β-decay spectroscopy [5, 6], deep inelastic scattering [7] and Coulomb-excitation [8, 9] experiments all claim to have evidence for a sub-shell closure at $N = 32$. By extending our knowledge to ^{54}Ca and other isotopes in this region, it might be possible to learn more about both this potential shell gap and look for a possible closure at $N = 34$.
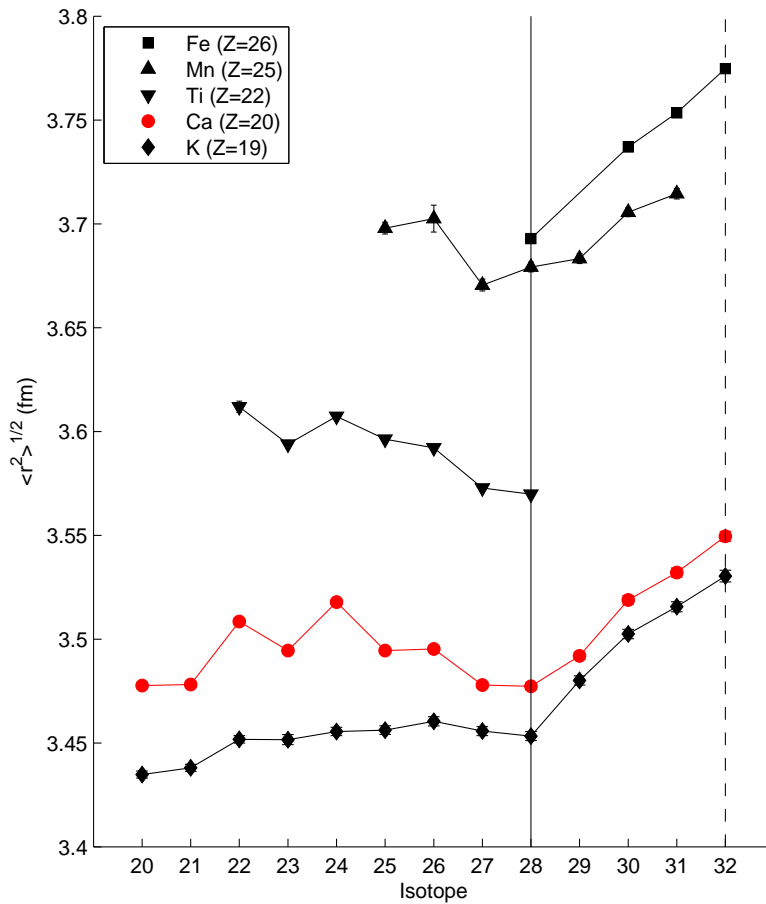

Figure 6.5: The updated root mean square charge radii $\langle r^2 \rangle^{1/2}$ for the calcium region [59, 60, 61]. Systematic errors were not taken into account. When approaching $N = 32$, the slope does not tend to stagnate. Therefore, no evidence for a shell gap at $N = 32$ is observed.

6.2 Hyperfine parameters and spin determination of ^{51}Ca

In this section the spin of ^{51}Ca is determined using the A-ratio. Afterward the final numbers of the hyperfine parameters are presented.

6.2.1 Determination of the spin of ^{51}Ca

As mentioned before the hyperfine parameters are obtained by fitting the number of counts as a function of the frequency with a Voigt profile (equation (5.2)). From this, the A-ratio, defined as $A(^2S_{1/2})/A(^2P_{3/2})$, can be calculated. Of course the fit, and thus the hyperfine parameters, depend on the spin. Therefore it is important to determine the spin of ^{51}Ca before calculating final numbers.

As can be seen from Table 6.5, the ratio of the A parameters $A(^2S_{1/2})/A(^2P_{3/2})$ is constant within error bars, as expected for an isotopic chain [44]. Note that this ratio is only constant when the hyperfine anomaly is neglected. Since the A-ratio of an isotope depends on the spin, it is possible to determine the spin of ^{51}Ca using the A-ratio.

Isotope	A-ratio
43	25.97(20)
45	25.89(16)
47	25.77(17)
49	25.951(46)
Mean	25.936(42)

Table 6.5: Ratio of A parameters for every isotope. The A-ratio is defined as $A(^2S_{1/2})/A(^2P_{3/2})$.

The spin/parity of ^{51}Ca is expected to be $3/2^-$ [3], which would correspond with a hole in the $2p_{3/2}$ neutron orbital. To narrow down the possible spins, the number of peaks in a typical ^{51}Ca spectrum should be counted. From Figure 6.6, it is easily confirmed that this spectrum has 6 peaks. Therefore, the spin can be 3/2, 5/2 or 7/2. To deduce the correct spin, the experimental A-ratio value for every isotope is plotted in Figure 6.7. In case of ^{49}Ca and ^{51}Ca, the fitting is done for all three possible spins, and different A-ratios are obtained. Since this ratio is expected to be constant over the odd Ca isotopes, the spin must be 3/2 for both isotopes.
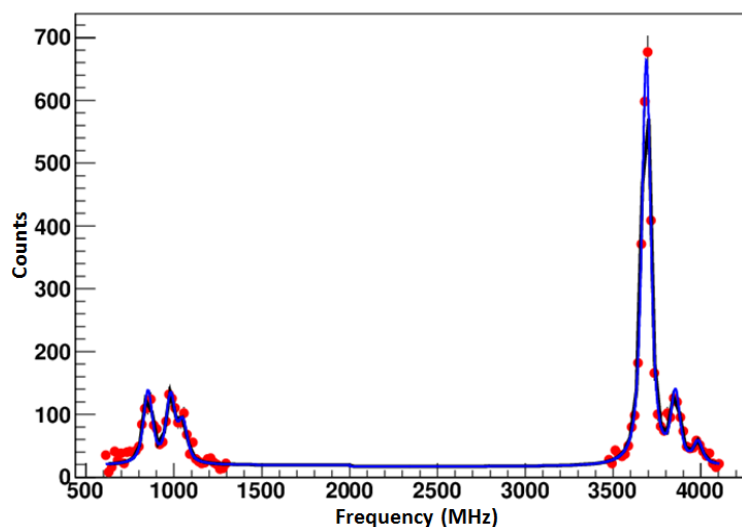
Figure 6.6: The fitted spectrum of ^{51}Ca, run 139, both multiplets. The spectrum has 6 peaks, which gives three options for the spin: 3/2, 5/2 or 7/2.
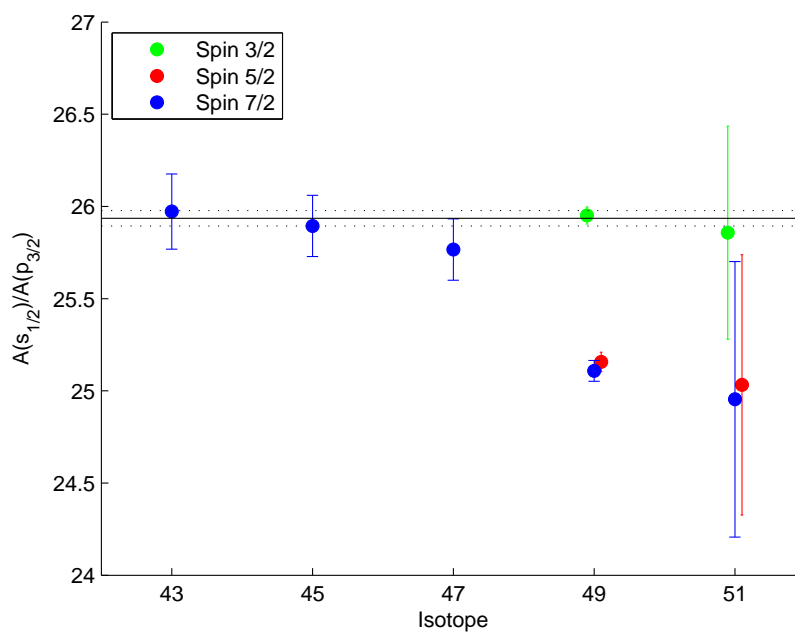

Figure 6.7: The $A(^2S_{1/2})$ over $A(^2P_{3/2})$ ratio for every odd Ca isotope. For ^{49}Ca and ^{51}Ca, the fitting was done with three possible spins. It is clear that in both cases spin 3/2 has the best agreement.

6.2.2 Hyperfine parameters

Since the spin of ^{51}Ca is now determined, hyperfine parameters for all isotopes can be obtained. It is possible to limit the number of free parameters and thus reduce the error, by fitting all spectra with a fixed A-ratio. Therefore, the mean A-ratio was calculated to be 25.936(42). New values for the hyperfine parameters using this fixed A-ratio were obtained by fitting every file once more. These are within error bars of the free A-ratio values. All hyperfine parameters can be found in Table 6.6.

The systematic errors on the hyperfine parameters were estimated in the same way as before. Even when all possible causes of systematic errors (ISCOOL voltage calibration, Kepco factor, laser wavelength and ion mass) are taken into account, the maximal systematic error for $A(^2S_{1/2})$ is 0.02 MHz, which is less than 10% of the statistical error. Therefore the systematic errors negligibly small.

6.3 Nuclear moments

The nuclear moments can be calculated from the hyperfine parameters as was explained in section 3.3. In the first part of this section the magnetic moments are discussed. The experimental g-factors are compared to theoretically calculated single particle g-factors to gain information about the composition of the wave function of the ground state of the calcium isotopes. The magnetic moments are also compared to literature values and calculations with the TBLC8 interactions, executed by van der Merwe *et al.* [23]. In the second part the quadrupole moments are discussed and compared to literature. An effective single particle quadrupole moment is deduced and experimental values are compared to theoretical calculations. At the end of this chapter, an overview of the hyperfine parameters and nuclear moments is given in Table 6.13.

6.3.1 Magnetic moments and g-factors

The results for the magnetic moments of all measured calcium isotopes can be found in Table 6.7. Note that systematic errors are again negligible. Values for both free and fixed A-ratio are given and agree very well. In the rest of the discussion and in the figures, the free A-ratio values are used. In Figure 6.8 our experimental results are compared to literature. A good agreement is observed.

Isotope	$A(^2S_{1/2})$ **(MHz)**		
	free	fixed	literature
43	-806.96(54)	-807.09(42)	-806.4020716(8) [27]
			-805(2) [30]
45	-812.16(42)	-812.08(28)	-
47	-861.16(34)	-860.75(22)	-
49	-1971.13(33)	-1971.12(24)	-
51	-1501.2(1.3)	-1499.4(1.1)	-

Isotope	$A(^2P_{3/2})$ **(MHz)**		
	free	fixed	literature
43	-33.42(22)	-33.183(10)	-31.9(2) [30]
			-31.0(2) [29]
45	-31.36(20)	-31.304(12)	-
47	-33.42(22)	-33.183(10)	-
49	-75.96(13)	-75.992(62)	-
51	-58.1(1.3)	-57.81(90)	-

Isotope	B **(MHz)**		
	free	fixed	literature
43	-4.8(1.9)	-4.9(1.9)	-6.7(1.4) [30]
			-6.9(1.7) [29]
45	2.6(1.3)	2.5(1.3)	-
47	12.5(1.4)	12.5(1.5)	-
49	-5.58(0.94)	-5.6(1.8)	-
51	4.9(3.8)	6.0(3.0)	-

Table 6.6: Overview of the final hyperfine parameters. Both the values with a free and fixed A-ratio are given, together with the most important literature values. Systematical errors on the hyperfine parameters are estimated less than 10% of the errors quoted in the table, and are therefore negligible.

Isotope	μ (μ_N)		
	free	fixed	literature
43	-1.31855(89)	-1.31877(68)	-1.317643(7) [28]
			-1.3173(6) [65]
45	-1.32705(68)	-1.32692(45)	-1.3274(14) [63]
			1.316(16) [52]
47	-1.40712(55)	-1.40644(36)	-1.38(14) [52]
49	-1.38033(23)	-1.38033(17)	-
51	-1.05122(93)	-1.04996(77)	-

Table 6.7: Experimental magnetic moments for all calcium isotopes, together with the most important literature values.
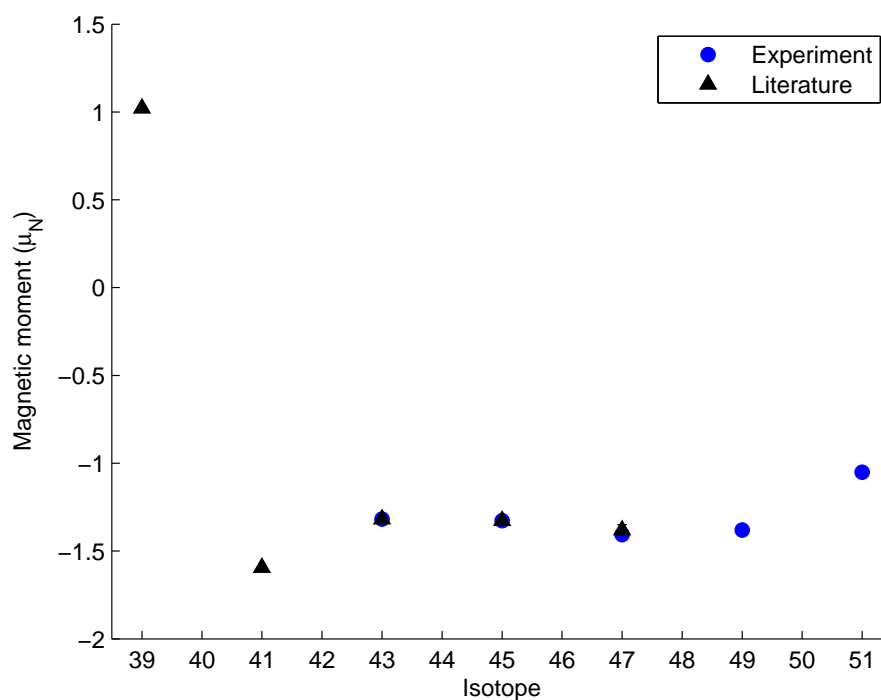

Figure 6.8: Magnetic moments from this experiment and from literature ([62, 63, 28, 52]). There is a good agreement between literature and experiment.

To gain more insight into the wave function of the ground state of the Ca isotopes, the experimental values are compared to shell model calculations. Such calculations should be able to reproduce experimental observables, and to predict properties that were not measured yet. Therefore it is necessary to choose an appropriate core as a shell model basis and a valid model space in which the valence nucleons can interact. In order to find this, theorists use experimentally obtained energy levels and binding energies [26]. The base inputs are calculated two body matrix elements for all possible combinations of nucleon orbitals in the model space, and the single particle energies that were (in most cases) obtained experimentally.

In this work, the experimental results are compared to the calculations done by van der Merwe, Richter and Brown using the TBLC8 interaction [23]. This is a two body interaction with a ^{40}Ca core and a model space consisting of the $1f_{7/2}$, $2p_{3/2}$, $1f_{5/2}$ and $2p_{1/2}$ orbitals. The only restriction is that maximum one particle can be excited from $1f_{7/2}$ to a higher orbital. The two body matrix elements from the pf shell were fitted to 494 energy levels in the $A = 41 - 66$ region. It is especially suited to reproduce low lying energy levels and ground state nuclear moments in this region.

To calculate the magnetic moment, van der Merwe *et al.* used the following free and effective g-factors:

$$\begin{array}{l} \text{For protons: } g_l = 1 \text{ , } g_s = +5.586 \text{ (free) and } g_s = +5.031 \text{ (effective) [23]} \\ \text{For neutrons: } g_l = 0 \text{ , } g_s = -3.826 \text{ (free) and } g_s = -3.041 \text{ (effective) [23]} \end{array} \tag{6.1}$$

With this information it is possible to calculate the g-factor for a certain nucleon orbital, and compare it to the experimental g-factors, calculated by dividing the magnetic moment by the spin. If a good agreement is found between experiment and theory, it means that the calculated wave function is close to the real one, thus information on the configuration of the ground state can be obtained.

The g-factor for a certain nucleon orbital can be calculated using equation (3.4) to calculate the Schmidt value. By dividing this $\mu_{\text{s.p.}}(j)$ with the spin j of the single particle state, the g-factor can be obtained. Ca isotopes contain 20 protons, which is a magic number. This means that the g-factor is only determined by the unpaired neutrons. Calculated numbers can be found in Table 6.8 and were plotted as lines in Figure 6.9 to compare with experimental values.
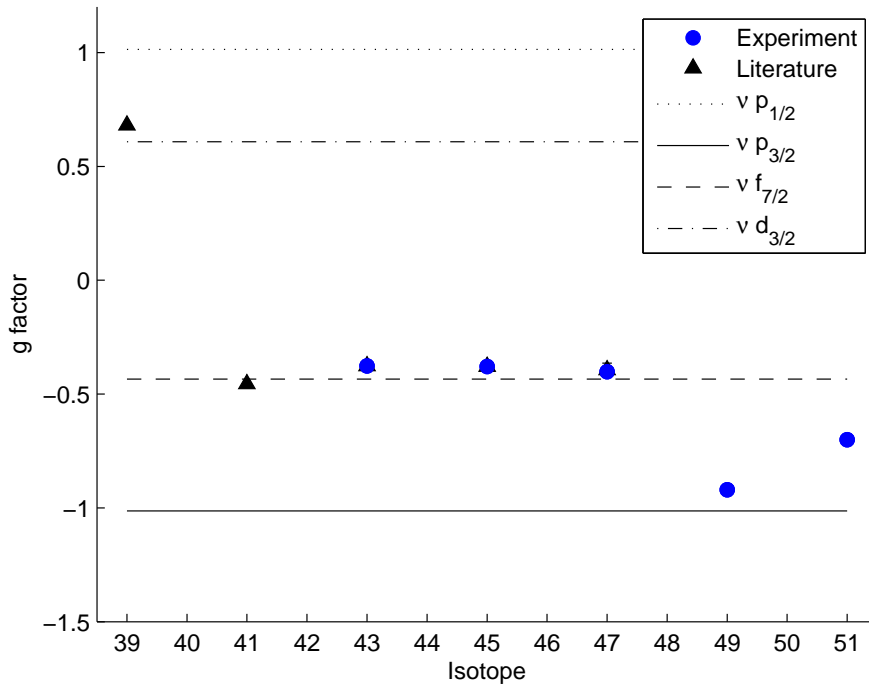
Figure 6.9: The calculated single particle g-factors from equation (3.4), using the effective values for the orbital and spin g-factors from the TBLC8 interaction [23], equation (6.1). The calculated g-factors are shown in Table 6.8. The experimental g-factors for ^{39}Ca and ^{41}Ca were obtained from [62] and [63] respectively.

It turns that out the hole in the $\nu d_{3/2}$ orbit gives ^{39}Ca a very single particle like nuclear moment. When adding neutrons, the $\nu f_{7/2}$ and $\nu p_{3/2}$ orbits are filled. Also for $^{41-47}$Ca a very good agreement with the single particle g-factor is found. The experimental g-factor of ^{49}Ca is very close to the effective g-factor for $p_{3/2}$, as one would expect. For ^{51}Ca, a deviation from the single particle value is found. This suggests that the ground state wave function is not a pure single particle configuration, unlike the other isotopes. ^{51}Ca has 3 neutrons outside the $N = 28$ shell. A gradual filling would lead to a $(\nu p_{3/2}^3)_{3/2^-}$ ground state wave function with $g(3/2^-) = g_{\text{s.p.}}(p_{3/2})$. As the observed value deviates from this value, mixing of other configurations occurs in this wave function. This can be $((\nu p_{3/2}^2)_2 \nu p_{1/2}^1)_{3/2^-}$ or $((\nu p_{3/2}^2)_2 \nu f_{5/2}^1)_{3/2^-}$. Both have 3 unpaired neutrons (seniority $\sigma = 3$ configurations), with an unpaired neutron in $\nu p_{1/2}$ or $\nu f_{5/2}$ coupling to a neutron pair coupled to 2^+. More theoretical calculations and modeling is needed to determine the amount of mixing in the ground state wave function.

Neutron orbit	g_{free}	$g_{\text{effective}}$
$f_{7/2}$	-0.547	-0.434
$p_{3/2}$	-1.275	-1.014
$f_{5/2}$	0.547	0.434
$d_{3/2}$	0.765	0.608

Table 6.8: Free and effective g-factors for the suitable neutron orbits, calculated with equations (3.4) and (6.1) and plotted in Figure 6.9.

Now the nuclear magnetic moments can be compared to the calculated values using the TBLC8 interaction. This was done in Figure 6.10 and Table 6.9. The theoretically calculated values and the experimental values are not in agreement within error bars. Nevertheless there is a relatively good agreement observed for the trend, except for ^{51}Ca. This suggests that the calculated wave function for ^{51}Ca is too pure, and more mixing is needed to reproduce the experimental value. The calculated free magnetic moments generally underestimate the experimental values, with another exception for ^{51}Ca, where μ is overestimated.

Isotope	μ_{free}	μ_{eff}	μ_{exp}
41	-1.913	-1.520	1.5942(7)
43	-1.712	-1.408	-1.31855(89)
45	-1.657	-1.317	-1.32705(68)
47	-1.591	-1.264	-1.40712(55)
49	-1.722	-1.368	-1.38033(23)
51	-0.6916	-0.5497	-1.05122(93)

Table 6.9: Overview of the magnetic moments calculated by van der Merwe *et al.* [23], in units of μ_N. The used free and effective g-factors can be found in equation (6.1). For comparison, the experimental values are also included in the table. The value for ^{41}Ca is obtained from a combined radiofrequency laser saturation spectroscopy experiment [63].
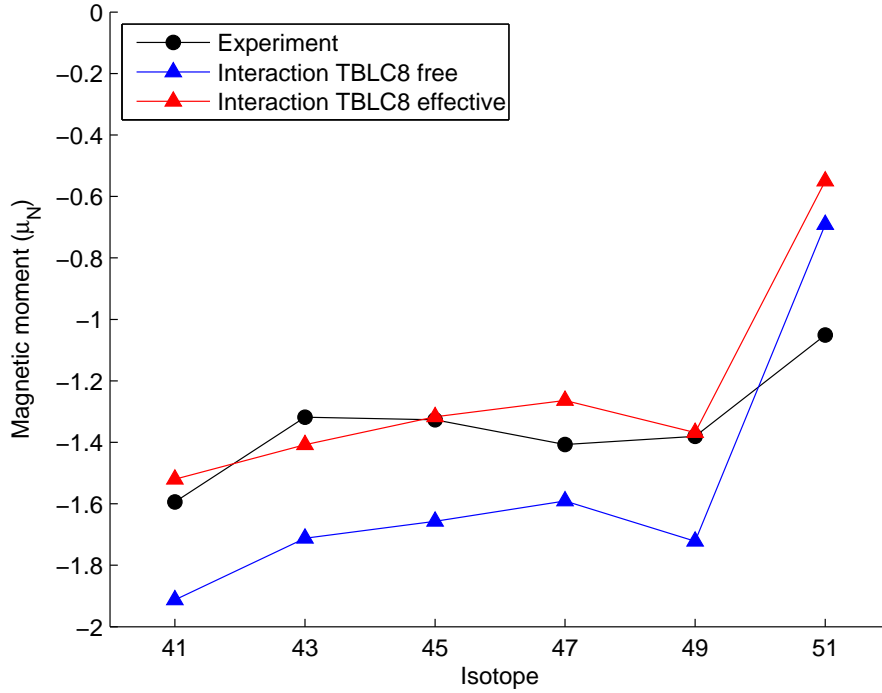
Figure 6.10: Comparison between the calculated magnetic moments using TBLC8 [23] (Table 6.9) and the results from our experiment, together with the results for ^{41}Ca from a combined radiofrequency laser saturation spectroscopy experiment [63]. The values for the g-factors can be found in equation (6.1).

6.3.2 Quadrupole moments

The final experimental quadrupole moments can be found in Table 6.10, together with some literature values. Note that the value by Silverans *et al.* is recalculated with the same hyperfine B factor as was used in this analysis. Systematic errors are negligible. Free and fixed A-ratio values are in agreement, and free values are used in the figures and the discussion. Our experimental quadrupole moments and literature values are plotted in Figure 6.11.

Isotope	Q (b)		
	free	fixed	literature
43	-0.031(13)	-0.032(13)	-0.0408(8) [31]
			-0.044(11) [30]
45	0.0167(89)	0.0159(88)	0.046(14) [63]
47	0.081(15)	0.081(15)	-
49	-0.0362(82)	-0.036(13)	-
51	0.032(25)	0.039(20)	-

Table 6.10: Experimental quadrupole moments for all calcium isotopes, together with the most important literature values.
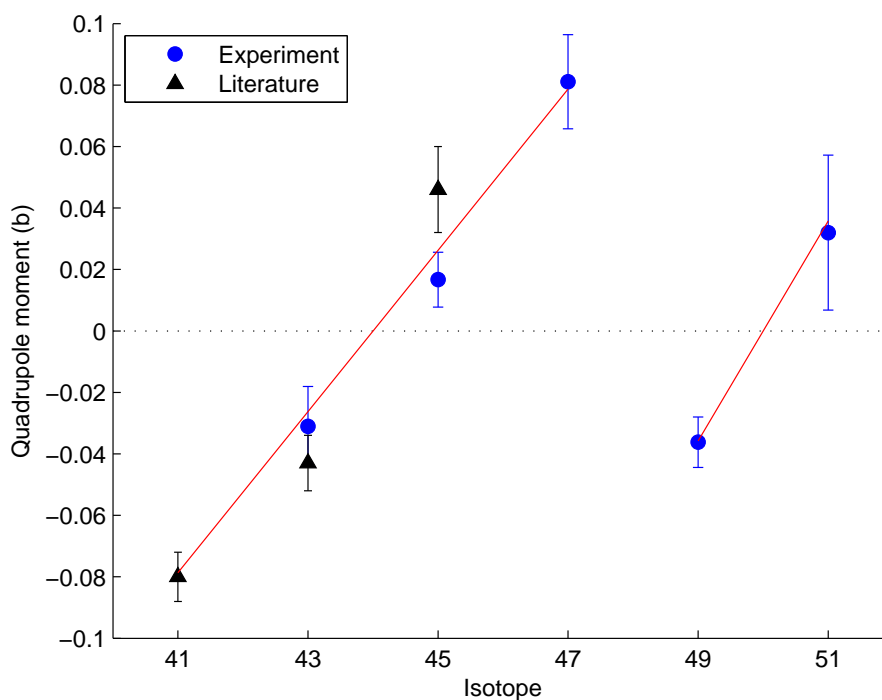

Figure 6.11: Quadrupole moments from this experiment and from literature ([64, 63, 30]). For ^{45}Ca there is no agreement. Quadrupole moments in the same neutron orbital are lying on a straight line.

It is clear from Figure 6.11 that quadrupole moments in the same neutron orbital are lying on a straight line. The nuclei go from a very oblate ($Q < 0$) to a very prolate shape ($Q > 0$) when neutrons are added. When an orbital is half filled, the quadrupole moment approaches zero. By determination of the slope of the quadrupole moments, the effective single particle quadrupole moment in equation (3.5) can be obtained using the seniority scheme [22]. This means that we can experimentally determine $Q_{s.p.}^{\text{eff}}$ for some orbital j in

$$Q = \frac{2j + 1 - 2n}{2j + 1 - 2\nu} Q_{s.p.}^{\text{eff}}$$

where n is the number of particles in the j orbital, and ν is the seniority. The seniority is the number of unpaired nucleons in the j orbital. In the case of Ca, ν always equals one. It is obtained that

$$Q_{s.p.}^{\text{eff}}(f_{7/2}) = -0.080(7) \text{ b} \tag{6.2}$$

$$Q_{s.p.}^{\text{eff}}(p_{3/2}) = -0.034(8) \text{ b} \tag{6.3}$$

Note that $Q_{s.p.}^{\text{eff}}$ is the product of the free single particle quadrupole moment and the effective charge. The quadrupole moments calculated with these effective charges are plotted as a straight line in Figure 6.11.

As with the magnetic moments, the quadrupole moments can be compared to the calculations done by van der Merwe *et al.* using the TBLC8 interaction [23]. The effective charges used in these calculations are given in Table 6.11, and calculated quadrupole moments can be found in Table 6.12 where they are compared to experimental values.

Interaction	e_n	e_p
TBLC8 (1)	0.5	1.5
TBLC8 (2)	0.84	1.486

Table 6.11: Effective charges for interaction TBLC8, used in [23]. Values are in units of the elementary charge e.

As can be seen from Figure 6.12, the agreement of the quadrupole moments is very good. With the effective charges $e_\mu = 0.5e$ and $e_\pi = 1.5e$, the trend in the experimental moments is rather well reproduced. The slope of the trend of the calculated values is somewhat lower than the slope in the experimental values for the $f_{7/2}$ orbit. On the other hand, with a larger neutron effective charge of $e_\mu = 0.84$, the slope is strongly overestimated. From this we can calculate that the neutron effective charge is a little larger than $0.5e$. Note that the change

in absolute value of the quadrupole moment from ^{47}Ca to ^{49}Ca is another clear evidence for the shell gap at $N = 28$. By measuring the quadrupole moment of ^{53}Ca in some future experiment it might be possible to obtain more information about a potential shell gap at $N = 32$.

Isotope	$Q_{\mathbf{TBLC8(1)}}$	$Q_{\mathbf{TBLC8(2)}}$	$Q_{\mathbf{exp}}$
41	-0.05681	-0.09545	-0.080(8)
43	-0.02076	-0.03487	-0.031(13)
45	0.02143	0.03600	0.0167(89)
47	0.07469	0.1255	0.081(15)
49	-0.03687	-0.06194	-0.0362(82)
51	0.04684	0.07869	0.032(25)

Table 6.12: Overview of the quadrupole moments calculated by van der Merwe *et al.* [23]. The used effective charges can be found in Table 6.11. For comparison, the experimental values are also included in the table. The value for ^{41}Ca is obtained from a combined radiofrequency laser saturation spectroscopy experiment [63]. Quadrupole moments are in barns.
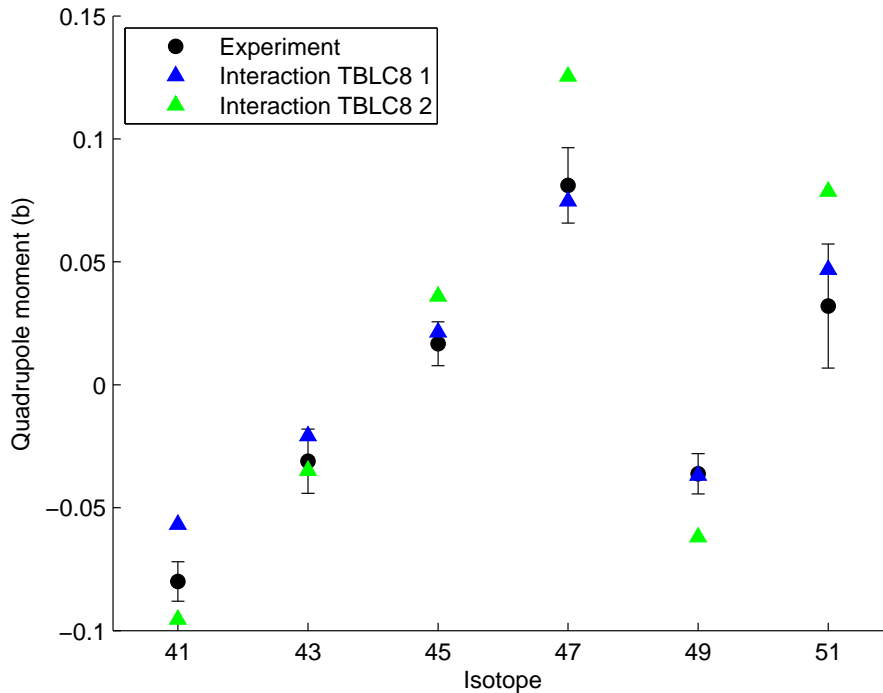

Figure 6.12: Comparison between the calculated quadrupole moments using TBLC8 [23] (Table 6.12) and the results from our experiment, together with the results for ^{41}Ca from a combined radiofrequency laser saturation spectroscopy experiment [63]. The used effective charges can be found in Table 6.11.

Isotope	$A(^2S_{1/2})$ (MHz)			$A(^2P_{3/2})$ (MHz)			B (MHz)		
	free	fixed	literature	free	fixed	literature	free	fixed	literature
43	-806.96(54)	-807.09(42)	-806.4020716(8) [27] -805(2) [30]	-33.42(22)	-33.183(10)	-31.9(2) [30] -31.0(2) [29]	-4.8(1.9)	-4.9(1.9)	-6.7(1.4) [30] -6.9(1.7) [29]
45	-812.16(42)	-812.08(28)	-	-31.36(20)	-31.304(12)	-	2.6(1.3)	2.5(1.3)	-
47	-861.16(34)	-860.75(22)	-	-33.42(22)	-33.183(10)	-	12.5(1.4)	12.5(1.5)	-
49	-1971.13(33)	-1971.12(24)	-	-75.96(13)	-75.992(62)	-	-5.58(0.94)	-5.6(1.8)	-
51	-1501.2(1.3)	-1499.4(1.1)	-	-58.1(1.3)	-57.81(90)	-	4.9(3.8)	6.0(3.0)	-

Isotope	μ (μ_N)			Q (b)		
	free	fixed	literature	free	fixed	literature
43	-1.31855(89)	-1.31877(68)	-1.317643(7) [28] -1.3173(6) [65]	-0.031(13)	-0.032(13)	-0.0408(8) [31] -0.044(11) [30]
45	-1.32705(68)	-1.32692(45)	-1.3274(14) [63] 1.316(16) [52]	0.0167(89)	0.0159(88)	0.046(14) [63]
47	-1.40712(55)	-1.40644(36)	-1.38(14) [52]	0.081(15)	0.081(15)	-
49	-1.38033(23)	-1.38033(17)	-	-0.0362(82)	-0.036(13)	-
51	-1.05122(93)	-1.04996(77)	-	0.032(25)	0.039(20)	-

Table 6.13: Overview of all hyperfine parameters, magnetic moments and quadrupole moments. Both the values with a free and fixed A-ratio are given, together with the most important literature values. Systematical errors on the hyperfine parameters are estimated less than 10% of the errors quoted in the table, and are therefore negligible.

Chapter 7

Conclusion

The ground state properties of neutron rich calcium nuclei ($Z = 20$) were measured using bunched-beam collinear laser spectroscopy at the COLLAPS beam line of ISOLDE, CERN in April 2012. These properties contain the spin, nuclear moments and differences in charge radii of $^{40,43-52}$Ca. By bunching the ion beam and putting correlated gates on the detection time of the photomultiplier tubes, background was suppressed by a factor 10^4 and a high sensitivity was obtained.

The isotope shifts and mean square charge radii of $^{43-52}$Ca were measured relative to ^{40}Ca. Values were in excellent agreement with the literature values from Vermeeren *et al.* [45] and were acquired with a higher precision. For the first time differences in charge radii of ^{49,51,52}Ca were measured. The electronic factor and specific mass shift constant were obtained using the method of Mårtensson-Pendrill's group [46] and were acquired with a higher precision than in their work. Using the newly obtained values for F and K_{SMS}, differences in mean square charge radii could be recalculated with yet a smaller uncertainty.

Hyperfine A and B factors of odd-even Ca isotopes were determined, and nuclear moments were calculated both with fixed and free A-ratio. All obtained nuclear moments were in agreement with literature values inside error bars. The magnetic moment of ^{49,51}Ca and the quadrupole moment of ^{47,49,51}Ca were measured successfully for the first time. Results were compared to theoretical calculations with the TBLC8 interaction by van der Merwe *et al.* [23]. A clear deviation in the calculated magnetic moment of ^{51}Ca was observed, suggesting a considerable configuration mixing in the ^{51}Ca ground state. The quadrupole moments fitted

experimental values quite well.

The ground state spin of ^{51}Ca was never determined directly from an experiment before. As Novoselsky *et al.* [3] expected, the spin/parity is confirmed to be $3/2^-$. This corresponds with one hole in the $\nu 2p_{3/2}$ orbital. Nevertheless, mixing with other states has to be taken into account considering that the experimental g-factor deviates from the $\nu 2p_{3/2}$ single particle value. Further research on this subject is necessary.

The results of the experiment were discussed in terms of the nuclear structure and the shell model. Clear evidence for a shell gap at $N = 28$ confirmed the proven magical number. Indications of an expected sub-shell closure at $N = 32$ were not observed. In the future more reliability on this matter should be acquired by measuring more exotic isotopes in the Ca region, for example ^{53}Ca and ^{54}Ca. From this, a possible shell gap at $N = 34$ might also be examined. Nevertheless this will require some adaptations in the setup, as the optical detection setup is not suited beyond ^{52}Ca. The feasibility of a setup based on radioactive detection of optically pumped ions after state-selective charge exchange (ROC) will be investigated in the following years [14].

Bibliography

[1] HEYDE, K. 1994. *The Nuclear Shell Model.* Springer-Verlag.

[2] *Evaluated Nuclear Structure Data File (ENSDF) Retrieval* on http://www.nndc.bnl.gov/ensdf/.

[3] NOVOSELSKY, A., VALLIERES, M., LA'ADAN, O., 1997. *Full $f-p$ Shell Calculation of ^{51}Ca and ^{51}Sc.* Phys. Rev. Letters Vol. 79, 22.

[4] GADE, A., GLASMACHER, T. 2008. *In-beam nuclear spectroscopy of bound states with fast exotic ion beams.* Progress in Particle and Nuclear Physics 60, pp 161-224.

[5] PRISCIANDARO, J.J. *et al.* 2001. *New evidence for a subshell gap at $N = 32$.* Phys. Let. B 510, 17-23.

[6] LIDDICK, S.N. *et al.* 2004. *Development of shell closures at $N = 32, 34$: $\beta-decay$ of neutron-rich Sc isotopes.* Phys. Rev. C, 064303.

[7] JANSSENS, R.V. F. *et al.* 2002. *Structure of $^{52,54}Ti$ and shell-closures in neutron-rich nuclei above ^{48}Ca.* Phys. Let. B 546, 55-62.

[8] DINCA, D.C. 2005. *Reduced transition probabilities to the first 2^+ state in $^{52,54,56}Ti$ and development of shell closures at $N = 32, 34$.* Phys. Rev. C 71, 041302(R).

[9] BURGER, A. *et al.* 2005. *Relativistic Coulomb excitation of neutron-rich $^{54,56,58}Cr$: On the pathway of magicity from $N = 40$ to $N = 32$.* Phys. Let. B 622, 29-34.

[10] HONMA, M., OTSUKA, T., BROWN, B.A. and MIZUSAKI, T., 2002. *Effective interaction for pf-shell nuclei.* phys. rev. C, Vol. 65, 061301.

[11] POVES, A., SANCHEZ-SOLANO, J., CAURIER, E., NOWACKI, F. 2001. *Shell model study of the isobaric chains A = 50, A = 51 and A = 52.* Phys. A 694, 157, Elsevier.

[12] MAIERBECK, P. *et al.* 2009. *Structure of ^{55}Ti from relativistic one-neutron knockout.* Physics Letters B 675 pp 22-27.

[13] BEINER, M., LOMBARD, R.J., MAS, D., 1975. *Self-consitent calculations of ground state properties for unstable nuclei.* Nuclear Physics A249, pp1-28.

[14] BISSEL, M.L. *et al.* 2011. *Proposal to the ISOLDE and Neutron Time-of-Flight Committee: Spins, Moments and Charge Radii Beyond ^{48}Ca.*

[15] HONMA, M., OTSUKA, T., BROWN, B.A. and MIZUSAKI, T., 2005. *Shell-model description of neutron-rich pf-shell nuclei with a new effective interaction GXPF1.* Eur. Phys. J. A 25, 499.

[16] BISSEL, M.L. *et al.* 2011. *Addendum to the ISOLDE and Neutron Time-of-Flight Committee: Ground-state properties of K-isotopes from laser and β-NMR spectroscopy.*

[17] CHEAL, B. 2010. *Proposal to the 38th meeting of the INTC: Collinear laser spectroscopy of manganese isotopes using optical pumping in ISCOOL.*

[18] KRANE, K.S. 1987. *Introductory Nuclear Physics.* John Wiley and Sons.

[19] BOHR, A. and MOTTELSON, B.R. 1969. *Nuclear Structure, Vol. I.* Benjamin, New York.

[20] NEUGART, R. and NEYENS, G. 2006. *Nucear Moments.* Lecture Notes Phys. 700, pp 135-189. Springer-Verlag Berlin Heidelberg.

[21] CASTEL, B. and TOWNER, I.S. 1990. *Modern Theories of Nuclear Moments.* Oxford.

[22] NEYENS, G. 2003. *Nuclear magnetic and quadrupole moments for nuclear structure research on exotic nuclei.* Reports on progress in physics 66, pp 633-689. IOP Publishing Ltd, UK.

[23] VAN DE MERWE, M.G., RICHTER, W.A. and BROWN, B.A. 1994. *Effective interactions for $A = 41 - 66$ nuclei.* Nuclear Physics A 579, pp 173-196.

[24] COTTENIER, S. and ROTS, M. 2005. *Hyperfine Interactions and their Applications in Nuclear Condensed Matter Physics: a microscopic introduction.* Springer.

[25] KING, W.H. 1984. *Isotope shifts in atomic spectra.* Plenum Press, New York.

[26] PAPUGA, J. 2011. *Laser spectroscopy of neutron-deficient odd-mass Cu isotopes.* Pre-doctoral Thesis, K.U. Leuven.

[27] ARBES, F. *et al.* 1994. *Precise determination of the ground state hyperfine structure splitting of ^{43}Ca II.* Z. Phys. D31, 27.

[28] LUTZ, O., SCHWENK, A., UHL, A. 1973. *Nuclear Magnetic Resonance Studies of ^{43}Ca.* Z. Naturforsch. 28a, 1534.

[29] NORTERHAUSER, W., BLAUM, K., ICKER, K., MULLER, P., SCHMITT, A., WENDT, K. and WICHE, B. 1998. *Isotope shifts and hyperfine structure in the $3d\ ^2D_J \to 4p\ ^2P_J$ transitions in calcium II.* Eur. Phys. J. D 2, pp 33-39.

[30] SILVERANS, R.E. *et al.* 1991. *Hyperfine Structure Constants of Ca II States $4s\ 2S_{1/2}$ and $4p\ 2P_{1/2}$, $4p\ 2P_{3/2}$ and the Nuclear Quadrupole Moment of ^{43}Ca.* Z.Phys. D18, 351.

[31] SUNDHOLM, D., OLSEN, J. 1993. *Finite Element Multiconfiguration Hartree-Fock Determination of the Nuclear Quadrupole Moments of Chlorine, Potassium, and Calcium Isotopes.* J.Chem.Phys. 98, 7152.

[32] PYYKKO, P. 2008. *Year-2008 nuclear quadrupole moments.* Molecular Physics Vol. 106, 19651974.

[33] *The ISOLDE facility* on http://isolde.web.cern.ch

[34] *ISOLDE - Isotope Separator On-Line : An alchemical factory for nuclear physics* on http://public.web.cern.ch/public/en/research/ISOLDE-en.html.

[35] KRAMER, J., 2010. *Construction and Commissioning of a Collinear Laser Spectroscopy Setup at TRIGA Mainz and Laser Spectroscopy of Magnesium Isotopes at ISOLDE (CERN).* Johannes Gutenberg-Universitat in Mainz.

[36] *COLLAPS: COLlinear LAser SPectroscopy @ ISOLDE-CERN* on http://collaps.web.cern.ch/collaps

[37] AYSTO, J., 2004. *CERNs longest serving experimental facility.* Physics Reports 403404, 459 469. Elsevier.

[38] FRANBERG, H. 2008. *Off-line commissioning of the ISOLDE cooler.* Nuclear Instruments and Methods in Physics Research B 266, 45024504.

[39] MOHR, P.J., TAYLOR, B.N., and NEWELL, D.B. 2011. *The 2010 CO-DATA Recommended Values of the Fundamental Physical Constants.* (Web Version 6.0: http://physics.nist.gov/cuu/Constants/index.html).

[40] SUGAR, J. and CORLISS, C. 1985. J. Phys. Chem. Ref. Data 14, Suppl. 2.

[41] AUDI, G., MENG, W. 2011. *Atomic mass evaluation 2011 (AME2011).* Private communication 2011 April.

[42] GALLANT, A.T. 2012. *New Precision Mass Measurements of Neutron-Rich Calcium and Potassium Isotopes and Three-Nucleon Forces.* Physical review letters 109, 032506.

[43] BARLOW, R.J. 1999. *Statistics: A Guide to the Use of Statistical Methods in the Physical Sciences.* John Wiley and Sons, Chichester, New York, Brisbane, Toronto, Singapore.

[44] VINGERHOETS, P. January 2011. *Nuclear structure of Cu isotopes studied with collinear laser spectroscopy.* Doctoral Thesis, K.U. Leuven.

[45] VERMEEREN, L., SILVERANS, R.E., LIEVENS, P. *et al.* 1992. *Ultrasensitive Radioactive Detection of Collinear Laser Optical Pumping: Measurement of the Nuclear Charge Radius of ^{50}Ca.* Phys. Rev. Letters 68, 11. pp 1679-1682.

[46] MARTENSSON-PENDRILL, A.M., VERMEEREN, L., SILVERANS, R.E., *et al.* 1992. *Isotope shifts and nuclear-charge radii in singly ionized $^{40-48}Ca$.* Phys. Rev. A 45, 7. pp 4675-4681.

[47] SILVERANS, R.E., VERMEEREN, L. *et al.* 1993. *The electronic field shift factor of the $4s^2 S_{1/2} - 4p^2 P_J$ transitions in CaII.* Hyperfine Interactions 78, pp 247-250.

[48] BLACK, J.H., WEISHEIT, J.C. and LAVIANA, E. 1972. *Oscillator Strengths and Ground-State Photoionization Cross-Sections for Mg^+ and Ca^+.* ApJ 177, 567.

[49] PALMER, C.W.P. *et al.* 1984. *Laser Spectroscopy of Calcium Isotopes.* J.Phys.(London) B17, 2197.

[50] PALMER, C.W.P. *et al.* 1982. *Isotope shift in calcium by two-photon spectroscopy.* J. Phys. B: At. Mol. Phys. 15, 993.

[51] BERGMANN, E. *et al.* 1980. *Nuclear Charge Distribution of Eight Ca-Nuclei by Laser Spectroscopy.* Z.Phys. A294, 319.

[52] ANDL, A. *et al.* 1982. *Isotope Shifts and Hyperfine Structure of the $4s^2$ $1S_0$-$4s4p$ $1P_1$ Transition in Calcium Isotopes.* Phys.Rev. C26, 2194.

[53] WOHLFAHRT, H.D. *et al..* 1981. *Nuclear Charge Distributions in $1f_{7/2}$-Shell Nuclei from Muonic X-Ray Measurements.* Phys.Rev. C23, 533.

[54] YORK, D. *et al.* 2004. *Unified equations for the slope, intercept, and standard errors of the best straight line.* Am. J. Phys. 72 (3). Matlab script by Travis Wiens, http://www.mathworks.nl/matlabcentral/fileexchange/26586-linear-regression-with-errors-in-x-and-y.

[55] ANGELI, I. *et al.* 2009. *N and Z dependence of nuclear charge radii* J. Phys. G: Nucl. Part. Phys. 36, 085102.

[56] KLEIN, A. *et al.* 1996. *Moments and Mean Square Charge Radii of Short-lived Argon Isotopes.* Nuclear Physics A 607, pp 1-22. Elsevier.

[57] AVOULEA, M. *et al.* 2011. *Nuclear charge radii and electromagnetic moments of radioactive scandium isotopes and isomers.* J. Phys. G: Nucl. Part. Phys. 38, 025104.

[58] BLAUM, K. *et al.,* 2008. *Nuclear moments and charge radii of argon isotopes between the neutronshell closures $N = 20$ and $N = 28$.* Nuclear Physics A 799, 30-45.

[59] Kreim, K. 2013. Private communication (not published yet).

[60] CHARLWOOD, W. 2010. *Ground state properties of manganese isotopes across the $N = 28$ shell closure.* Physics Letters B 690 346351.

[61] *Chart of nucleus shape and size parameters.* on http://cdfe.sinp.msu.ru/services/radchart/radmain.html.

[62] MINAMISONO, T. *et al.* 1976. *Measurement of the Magnetic Moment of ^{39}Ca by Use of a Polarized Proton Beam and NMR Detection.* Phys.Lett. 61B, 155.

[63] ARNOLD, M. 1983. *Nuclear Electric Quadrupole Moment of ^{41}Ca by Laser-RF Spectroscopy.* Z.Phys. A314, 303.

[64] MATSUTA, K. *et al.* 1999. *Quadrupole Moment of ^{39}Ca.* RIKEN-98, p.79.

[65] OLSCHEWSKI, L. 1972. *Messung der magnetischen Kerndipolmomente an freien ^{43}Ca-, ^{87}Sr-, ^{135}Ba-, ^{137}Ba-, ^{171}Yb- und ^{173}Yb-Atomen mit optischem Pumpen.* Z.Phys. 249, 205.